

Cosmology and Astrophysics from Relaxed Galaxy Clusters III: Thermodynamic Profiles and Scaling Relations

A. B. Mantz,^{1,2,3,4*} S. W. Allen,^{3,4,5} R. G. Morris,^{3,5} R. W. Schmidt⁶

¹*Department of Astronomy and Astrophysics, University of Chicago, 5640 South Ellis Avenue, Chicago, IL 60637, USA*

²*Kavli Institute for Cosmological Physics, University of Chicago, 5640 South Ellis Avenue, Chicago, IL 60637, USA*

³*Kavli Institute for Particle Astrophysics and Cosmology, Stanford University, 452 Lomita Mall, Stanford, CA 94305, USA*

⁴*Department of Physics, Stanford University, 382 Via Pueblo Mall, Stanford, CA 94305, USA*

⁵*SLAC National Accelerator Laboratory, 2575 Sand Hill Road, Menlo Park, CA 94025, USA*

⁶*Astronomisches Rechen-Institut, Zentrum für Astronomie der Universität Heidelberg, Mönchhofstrasse 12-14, D-69120 Heidelberg, Germany*

Accepted 2015 December 07

ABSTRACT

This is the third in a series of papers studying the astrophysics and cosmology of massive, dynamically relaxed galaxy clusters. Our sample comprises 40 clusters identified as being dynamically relaxed and hot (i.e., massive) in Papers I and II of this series. Here we consider the thermodynamics of the intracluster medium, in particular the profiles of density, temperature and related quantities, as well as integrated measurements of gas mass, average temperature, total luminosity and center-excluded luminosity. We fit power-law scaling relations of each of these quantities as a function of redshift and cluster mass, which can be measured precisely and with minimal bias for these relaxed clusters using hydrostatic arguments. For the thermodynamic profiles, we jointly model the density and temperature and their intrinsic scatter as a function of radius, thus also capturing the behavior of the gas pressure and entropy. For the integrated quantities, we also jointly fit a multidimensional intrinsic covariance. Our results reinforce the view that simple hydrodynamical models provide a good description of relaxed clusters outside their centers, but that additional heating and cooling processes are important in the inner regions (radii $r \lesssim 0.5 r_{2500} \approx 0.15 r_{500}$). The thermodynamic profiles remain regular, with small intrinsic scatter, down to the smallest radii where deprojection is straightforward (~ 20 kpc); within this radius, even the most relaxed systems show clear departures from spherical symmetry. Our results suggest that heating and cooling are continuously regulated in a tight feedback loop, allowing the cluster atmosphere to remain stratified on these scales.

Key words: galaxies: clusters: general – X-rays: galaxies: clusters

1 INTRODUCTION

Highly dynamically relaxed galaxy clusters represent a minority of the cluster population, but provide a key laboratory for learning about the physics of the intracluster medium (ICM) and its interaction with cluster galaxies and active galactic nuclei (AGN). Uniquely in these morphologically regular systems, the three dimensional, radial profiles of the thermodynamic properties of the ICM can be reconstructed with minimal uncertainties from projection effects. In addition, X-ray data can provide precise constraints on the mass profiles of these clusters under the assumption of hydrostatic

equilibrium. The latter feature comes at the expense of introducing some systematic uncertainty due to non-thermal support, but both simulations and direct calibration using weak gravitational lensing data show that the overall bias in *Chandra* X-ray mass estimates for relaxed clusters is small ($\lesssim 10$ per cent; Nagai et al. 2007; Applegate et al. 2016).

Constraints on mass profiles, in comparison with estimates of the mass within a single characteristic radius, enable a wider range of investigations. In general, they provide a way to identify dynamically comparable radii across clusters, yielding the most meaningful comparison of interesting features. More specifically, they allow the scaling relations of thermodynamic quantities to be investigated as a function of radius. Violations of the self-similar scaling predicted from

* E-mail: amantz@slac.stanford.edu

purely gravitational spherical collapse shed light on the astrophysics of the ICM, in particular the heating mechanism that prevents classical cooling flows from forming in relaxed clusters. While numerous studies have investigated the scaling relations of global cluster properties (for a review, see Giodini et al. 2013), there has not yet been a complete study of the scaling of cluster thermodynamic profiles, including the radial structure of their intrinsic scatter (though see Sayers et al. 2013).

Other papers in this series have focused on identifying a sample of massive, relaxed clusters (Mantz et al. 2015), exploiting measurements of their gas mass fractions at intermediate radii to constrain cosmology (Mantz et al. 2014b), and measuring the average bias of X-ray hydrostatic masses for these clusters (Applegate et al. 2016; hereafter, respectively, Papers I, II and IV). Here we assume a concordance Λ CDM cosmology (with parameters $h = 0.7$, $\Omega_m = 0.3$ and $\Omega_\Lambda = 0.7$) and present the thermodynamic profiles of our relaxed cluster sample, their scaling properties, and some related astrophysical results. We briefly review aspects of our sample selection and spectral analysis methods in Section 2. Section 3 discusses the additional statistical methodology used in this work, in particular for performing multivariate regression with intrinsic scatter and/or arbitrary measurement error distributions. In Section 4, we present the thermodynamic profiles of the cluster sample and discuss some of the immediate consequences of these measurements that are available without further model fitting. Section 5 presents scaling relations of the profiles, including the radial structure of their intrinsic scatter, as well as “traditional” scaling relations of globally measured quantities. We summarize these results in Section 6.

In this paper, we follow the convention of defining characteristic cluster masses and radii in terms of the critical density of the Universe at the cluster’s redshift,

$$M_\Delta = \frac{4}{3}\pi\Delta\rho_{\text{cr}}(z)r_\Delta^3, \quad (1)$$

where Δ is often referred to as the “overdensity”. With this definition, the self-similar predictions for the scaling of the thermodynamic ICM properties can be written (Kaiser 1986)

$$n(r_\Delta) \propto E(z)^2, \quad (2)$$

$$kT(r_\Delta) \propto [\Delta^{1/2}E(z)M_\Delta]^{2/3},$$

where n and kT are the number density and temperature of the ICM. Here $E(z) = H(z)/H_0$ is the Hubble parameter ($\propto \sqrt{\rho_{\text{cr}}(z)}$), normalized to its value at $z = 0$ for convenience. Note that, using Δ as a surrogate for cluster radius, the shape of the self-similar density profile is completely specified by the expression above, whereas the shape of the temperature profile is determined by the shape of the underlying mass profile. Expressions for the self-similar scaling of pressure, $P = nkT$, and pseudo-entropy, $K = kT/n^{2/3}$, follow directly from those above, as do the predicted scalings of quantities integrated within a given overdensity (for which we drop the explicit dependence on Δ):

$$M_{\text{gas}} \propto M_\Delta, \quad (3)$$

$$kT \propto [E(z)M_\Delta]^{2/3},$$

$$L \propto E(z)^{2+2\alpha/3}M_\Delta^{1+2\alpha/3}.$$

Here and throughout this work, we define L to be the intrinsic rest-frame *soft-band* X-ray luminosity of the ICM (specifically, energies of 0.1–2.4 keV). For the $kT > 5$ keV clusters in our data set, the soft-band luminosity within a fixed radius has a relatively mild dependence on temperature, $L \propto (kT)^\alpha$ with $\alpha \approx -0.13$. This is in contrast to the bolometric luminosity ($\alpha_{\text{bol}} \approx 1/2$), for which the corresponding self-similar scaling is $L_{\text{bol}} \propto E(z)^{7/3}M_\Delta^{4/3}$.¹

Where we employ log-normal probability distributions in this work, these are defined as Gaussian in the *natural* log of the argument, such that their standard deviations can be approximately thought of as a fractional scatter.

2 DATA SET AND SPECTRAL ANALYSIS

This work employs the same sample of 40 massive, dynamically relaxed clusters used to constrain cosmological models in Paper II. The identification of this sample is described in Papers I and II. Briefly, we searched the *Chandra* archive for morphologically regular clusters, as defined by a suite of image statistics designed specifically for the task. These measurements probe the sharpness of the cluster surface brightness peak, the alignment of a series of standard isophotes with one another, and the symmetry of those isophotes about a globally defined cluster center. In addition, a minimum temperature of 5 keV (excluding the core) is required.² The cluster sample is summarized in Table 1.

Our procedure for reducing and cleaning of the *Chandra* data is described in detail in Paper II. The only difference is that in this work we employ a more recent version of the *Chandra* analysis software and calibration files (specifically CIAO³ 4.6.1 and CALDB⁴ 4.6.2). This update, from CALDB 4.4.10 to 4.6.2, spans a relatively important change to the model of the contaminant affecting the *Chandra*-ACIS detectors that, at some level, affects the analysis of observations as far back as 2004.⁵ The update is, however, minor during the period when most of our data were observed. Comparing results from both versions of the analysis, we find a small (5 ± 5 per cent) reduction in temperatures on average, and negligible change in density measurements.⁶

Paper II also describes in detail our procedure for

¹ Note that the $2/3$ terms in the exponents of the L – M_Δ relation are identified with the slope of the kT – M_Δ relation, making these two scaling relations less than independent where departures from self-similarity are concerned (see discussion by Maughan 2014).

² This temperature threshold is motivated by the expectation from simulations that the bias and scatter introduced by the assumption of hydrostatic equilibrium should increase for low-mass clusters and groups, even after selecting the most relaxed systems (Nagai et al. 2007). Simulations also predict a mass dependence of the gas mass fraction for less massive clusters, which would complicate the cosmological analysis of Paper II.

³ <http://cxc.harvard.edu/ciao/>

⁴ <http://cxc.harvard.edu/caldb/>

⁵ http://cxc.cfa.harvard.edu/caldb/downloads/Release_notes/CALDB_v4.5.9.html

⁶ Note that the cosmological results presented in Paper II are insensitive to an overall bias in temperature, since in that work the overall normalization of cluster mass profiles is calibrated using weak gravitational lensing data (see also Paper IV). Subsequent CALDB updates as of this writing (through 4.6.10a) should have

Table 1. Names, redshifts and masses of the relaxed clusters in our sample (see Papers I and II). Masses are from this work, using an updated *Chandra* calibration compared with Paper II. Also shown are the clean exposure time from this re-processing, as well as the specific *Chandra* observations (OBSIDs) used.

Cluster	z	r_{2500} (kpc)	M_{2500} ($10^{14} M_{\odot}$)	exp. (ks)	OBSIDs
Abell 2029	0.078	648 ± 4	4.17 ± 0.08	118.9	891,4977,6101,10434,10435,10436,10437
Abell 478	0.088	620 ± 8	3.69 ± 0.15	129.4	1669,6102,6928,6929,7217,7218,7222,7231,7232,7233,7234,7235
PKS 0745–191	0.103	671 ± 7	4.74 ± 0.14	148.8	2427,6103,7694,12881
RX J1524.2–3154	0.103	483 ± 9	1.77 ± 0.10	40.9	9401
Abell 2204	0.152	689 ± 13	5.41 ± 0.30	90.1	499,6104,7940
RX J0439.0+0520	0.208	496 ± 15	2.14 ± 0.19	35.5	527,9369,9761
Zwicky 2701	0.214	472 ± 7	1.85 ± 0.08	111.3	3195,7706,12903
RX J1504.1–0248	0.215	699 ± 15	6.02 ± 0.38	39.9	4935,5793
Zwicky 2089	0.235	452 ± 12	1.66 ± 0.13	47.0	7897,10463
RX J2129.6+0005	0.235	558 ± 13	3.13 ± 0.22	36.7	552,9370
RX J1459.4–1811	0.236	554 ± 17	3.07 ± 0.29	39.6	9428
Abell 1835	0.252	657 ± 7	5.21 ± 0.16	183.6	496,6880,6881,7370
Abell 3444	0.253	549 ± 11	3.04 ± 0.19	35.7	9400
MS 2137.3–2353	0.313	476 ± 10	2.11 ± 0.13	50.9	928,5250
MACS J0242.5–2132	0.314	532 ± 31	2.96 ± 0.52	7.7	3266
MACS J1427.6–2521	0.318	449 ± 16	1.79 ± 0.19	41.3	3279,9373
MACS J2229.7–2755	0.324	471 ± 15	2.08 ± 0.20	25.8	3286,9374
MACS J0947.2+7623	0.345	608 ± 15	4.58 ± 0.34	49.0	2202,7902
MACS J1931.8–2634	0.352	573 ± 12	3.86 ± 0.24	104.0	3282,9382
MACS J1115.8+0129	0.355	561 ± 14	3.63 ± 0.27	44.3	3275,9375
MACS J1532.8+3021	0.363	554 ± 11	3.53 ± 0.20	102.4	1649,1665,14009
MACS J0150.3–1005	0.363	432 ± 16	1.67 ± 0.18	26.1	11711
MACS J0011.7–1523	0.378	526 ± 16	3.07 ± 0.29	49.2	3261,6105
MACS J1720.2+3536	0.391	529 ± 20	3.18 ± 0.35	51.7	3280,6107,7718
MACS J0429.6–0253	0.399	537 ± 36	3.35 ± 0.67	19.3	3271
MACS J0159.8–0849	0.404	617 ± 18	5.12 ± 0.45	62.6	3265,6106,9376
MACS J2046.0–3430	0.423	427 ± 16	1.73 ± 0.20	42.8	5816,9377
IRAS 09104+4109	0.442	518 ± 19	3.17 ± 0.35	69.0	10445
MACS J1359.1–1929	0.447	463 ± 27	2.27 ± 0.40	54.2	5811,9378
RX J1347.5–1145	0.451	809 ± 28	12.19 ± 1.28	206.5	506,507,3592,13516,13999,14407
3C 295	0.460	452 ± 22	2.15 ± 0.31	90.9	578,2254
MACS J1621.3+3810	0.461	501 ± 13	2.92 ± 0.23	129.3	3254,6109,6172,7720,9379,10785
MACS J1427.2+4407	0.487	477 ± 19	2.60 ± 0.32	50.8	6112,9380,9808,11694
MACS J1423.8+2404	0.539	482 ± 11	2.86 ± 0.19	122.7	1657,4195
SPT-CL J2331–5051	0.576	425 ± 22	2.05 ± 0.32	31.8	9333,11738
SPT-CL J2344–4242	0.596	568 ± 29	5.01 ± 0.78	10.7	13401
SPT-CL J0000–5748	0.702	420 ± 34	2.29 ± 0.56	28.4	9335
SPT-CL J2043–5035	0.723	385 ± 14	1.81 ± 0.19	73.3	13478
CL J1415+3612	1.028	316 ± 11	1.44 ± 0.15	349.1	4163,12255,12256,13118,13119
3C 186	1.063	330 ± 13	1.71 ± 0.21	213.8	3098,9407,9408,9774,9775

analysing X-ray spectra for the clusters in our sample. We perform deprojections of the intracluster medium under two sets of assumptions, respectively using the NFWMASS and PROJCT models in XSPEC.⁷ In the first analysis, we assume that the cluster mass (dark plus baryonic) is described by a Navarro et al. (1997, hereafter NFW) profile. The ICM is modeled as a series of concentric, isothermal shells, and is assumed to be in hydrostatic equilibrium. This analysis provides simultaneous constraints on the mass, temperature and gas density profiles of a given cluster, but has the disadvantage of over-constraining the temperature profile. That is, the shape and especially the precision of the resulting

temperature profile is largely driven by the shape of the surface brightness profile, which has much higher signal-to-noise than the temperature information available intrinsically in the spectra. Consequently, we use these results only for determining cluster mass profiles, as well as the covariance between mass and temperature measurements (see below).

For the thermodynamic measurements which are the focus of this work, we instead use the “non-parametric” analysis described in Paper II. This analysis also assumes spherical symmetry, but does not require hydrostatic equilibrium. The results therefore contain no information about the cluster mass, but by the same token they are independent of assumptions regarding the mass profiles, and hence do not over-constrain the temperature profiles. Note that there is negligible difference between the gas density pro-

no effect on our analysis, given that the data employed here were all observed prior to 2013 (see Paper I).

⁷ <http://heasarc.gsfc.nasa.gov/docs/xanadu/xspec/>

files recovered from the two fitting methods compared to the uncertainties.

The annuli in which we extract spectra to analyse are chosen to provide good signal-to-noise for measurements of the gas density. To constrain temperatures, a more demanding task, it is necessary to assume isothermality across groups of a few adjacent spherical shells. The effective resolution of our temperature profiles is thus lower than that of our density profiles from this analysis.⁸ Figure A1 in the appendix shows the temperature and density profiles measured for each of our clusters, from both of the analyses described above. As already mentioned, the temperature profiles can be more finely binned when hydrostatic equilibrium and a form for the mass profile are assumed. Note that the good agreement between temperature profiles from the two analyses verifies that the NFW profile-hydrostatic equilibrium model is a good description of the data, within measurement uncertainties.

Our primary results are based on the profiles shown in Figure A1. However, we also consider integrated (i.e. not radially resolved) thermodynamic measurements in Section 5.2. For these results, we use the same apparatus as the non-parametric model described above, but with some specializations. Specifically, this model has only two free temperatures, corresponding to the cluster volumes at radii $< 0.15 r_{500}$ and $> 0.15 r_{500}$, with r_{500} estimated from the NFW fit. The temperature in the outer radial bin is essentially identical to what we would obtain from a typical analysis of the spectrum in projection, but this approach allows the measurement covariance between this “center-excised” temperature, the projected luminosity, and the spherically integrated gas mass to be fully captured.

In Paper II, we identified for each cluster a central region that was excluded from the NFW model fits. By default, this was a circle of radius 50 kpc, although in some cases the excluded region is larger in order to encompass visible structure in the ICM.⁹ The motivation for excluding these data from the fit is to avoid biases due to local violations of hydrostatic equilibrium, gas inhomogeneities, asphericity, and any offset between the densest gas and the center used for deprojection (which was chosen based on the large-scale emission). Equilibrium is not a concern for our non-parametric fits, but the other issues above can potentially still bias the results of a spherical deprojection at small radii. In particular, we generically expect non-zero ellipticity or an offset of the deprojection center from the brightest pixel to result in an underestimate of the gas densities and/or overestimate of the temperatures at the smallest radii. In the following sections, we will present results from non-parametric fits which extend all the way into the cluster centers alongside (more robust) results where the central regions are discarded. Fits to the thermodynamic profiles will always use center-excluded data.

In Paper II, we calibrated our X-ray mass measurements to a standard provided by the Weighing the Giants weak lensing analysis (von der Linden et al. 2014; Kelly et al.

2014; Applegate et al. 2014). As detailed further in Paper IV, this correction factor is consistent with unity (0.96 ± 0.08), and is consistent with being constant as a function of mass. For simplicity, we therefore do not apply any lensing-based correction to the X-ray NFW masses in this work.

3 ADDITIONAL METHODOLOGY

At various points in the following sections, we fit model profiles and trends with mass and/or redshift. This section summarizes the approaches we employ in these analyses.

In Section 5.2, we constrain the multivariate scaling relations of X-ray luminosity, temperature and gas mass as a function of total mass and redshift for our sample. For this analysis, we approximate the measurement uncertainties on all quantities as log-normal, and the intrinsic scatter as a multi-dimensional log-normal distribution, so that the power law model for the scaling relations becomes a linear model in the transformed (logarithmic) variables. Covariances among the measured quantities are accounted for (see below), as well as covariances in the intrinsic scatter. Our fitting method is inspired by the work of Kelly (2007), who proposed an efficient Gibbs sampling algorithm for fitting a similar model with only one response variable. An associated paper (Mantz 2016) describes our implementation of a multivariate version of the Kelly (2007) algorithm, which is publically available as a package for R¹⁰ called LRGS.¹¹ Note that generic Markov Chain Monte Carlo algorithms have significant difficulty navigating the complex parameter space of the elements of a covariance matrix, at least in our experience, making the Gibbs sampling approach of LRGS potentially useful for multivariate regression in general.

The thermodynamic results that we present in this paper stem from the non-parametric spectral analysis described in the previous section. The uncertainties from that analysis directly reflect the statistical power of the data. However, in order to constrain scaling relations with mass for the entire sample of clusters, most of which do not have weak lensing data, we must use mass measurements from the hydrostatic NFW analysis. This introduces a dilemma without a perfect solution: we would like to use masses from the NFW analysis but, to avoid spuriously tight constraints, temperatures from the non-parametric analysis. At the same time, it is crucial to account for the covariance between mass and temperature introduced by the hydrostatic assumption, i.e. the fact that statistical fluctuations in temperatures also affect the measured masses. We deal with this issue for each cluster as follows. First, we identify posterior samples of total mass from the NFW analysis, sorted into increasing order, with samples of the other X-ray observables from the non-parametric analysis sorted into increasing-temperature order. At this point, the mass-temperature correlation coefficient from the list of samples is unity. We then randomly permute elements of the mass list until the mass-temperature covariance in this hybrid list of samples matches the mass-temperature covariance internal

⁸ We also leave metallicities free, although these must be binned even more coarsely than temperatures.

⁹ Point sources are always masked, regardless of their position within the cluster.

¹⁰ <http://www.r-project.org>

¹¹ <https://github.com/abmantz/lrgs>

to the NFW fit (as measured directly from the NFW posterior samples). The result of this procedure is a set of samples with marginal temperature variance matching that of the non-parametric fit, marginal mass variance matching the NFW fit, and with an orientation of the mass–temperature error ellipse that also matches the NFW fit. The internal covariance of gas mass, temperature and luminosity is unaffected by this process. Note that we implicitly assume negligible mass– M_{gas} and mass–luminosity correlations at fixed radius; certainly we do not expect strong correlations to be introduced by the hydrostatic assumption apart from that between mass and temperature (given the use of a soft-band luminosity; see Section 1).

In Section 5.1, we simultaneously fit a model for the mean scaled cluster density and temperature profiles, the intrinsic scatter between these profiles and internal to each as a function of radius, and the overall scaling of each profile with mass and redshift. The model is similar to the “Gaussian process” pressure profile model used by Sayers et al. (2013), consisting of a value for the mean profile at a set of scaled radii, the intrinsic covariance among profiles at those radii, and overall scalings with mass/redshift.¹² We expand on the Sayers et al. (2013) approach by marginalizing over uncertainty in the mass profile of each cluster. We use the same approach as above to account for the mass–temperature covariance, but in this case the mass affects not just the scaling of the density and temperature, but also the scaling of the ordinate that the mean profile is a function of, i.e. Δ or r/r_{2500} . As above, the intrinsic and measurement covariances are modelled as log-normal (now a function of radius). In practice, we interleave Metropolis steps for the global scaling parameters (the exponents in the scaling relations) with LRGS Gibbs samples of the mean profiles and intrinsic covariance.

4 THERMODYNAMIC PROFILES

To summarize the results of our non-parametric analysis for the entire cluster sample, Figure 1 shows “ensemble” profiles of electron density, temperature, pressure (nkT) and entropy ($kTn^{-2/3}$), after applying scalings from the Kaiser (1986) model. Dark and light shaded regions show, at each radius, the 68.3 and 95.4 per cent limits of the distribution of results for all clusters that provide data at that radius, reflecting both measurement uncertainty and intrinsic scatter. These figures thus represent the results in a minimally processed form, whereas estimates of the intrinsic, cluster-to-cluster scatter of the profiles require us to adopt and fit a model (see Section 5.1). The shaded part of each profile shows the results when the central region of each cluster is excluded, while unshaded lines show the continuation of the profiles into the cluster centers (see Section 2). Note that the entire cluster sample contributes to the ensemble at overdensities $\Delta > 10^3$; however, the number of clusters where we can confidently measure temperatures drops quickly at larger

radii, and results for $\Delta \lesssim 500$ should be particularly treated with caution.

In Figure 1, the thermodynamic profiles are plotted against two ordinates: the overdensity (Equation 1), and the physical radius in units of r_{2500} , both determined from the best fitting NFW profile for each cluster. The former is a natural choice for examining the scaling relations given in Equation 2, which in the self-similar model would hold at all Δ , and their intrinsic scatter.

The following subsections describe some of the qualitative features of these thermodynamic profiles, and compare them to results in the literature.

4.1 Density and Surface Brightness

The self-similar assumption of a constant gas-mass fraction with radius leads to a simple, mass-independent scaling for gas density at a given overdensity, $n \propto E(z)^2 \Delta$. Figure 1 shows that this relation approximately holds over a wide range in Δ ; the dashed line in the top-left panel corresponds to a power law $nE^{-2} \propto \Delta^{0.96}$, fit to the median center-excised profile. Qualitatively, we see that the self-similar expectation is approximately met over most of the volume probed, in particular in the center-excised region. The departure from a precise $\Delta^{1.0}$ scaling can be seen more clearly in the $f_{\text{gas}} = M_{\text{gas}}/M$ profiles presented in Paper II (Figures 2 and 3), specifically as a shallow increase of f_{gas} with radius.

The intrinsic scatter in scaled density profiles has immediate consequences for mass proxies based on the soft X-ray luminosity, the most straightforward quantity to estimate from shallow data. To demonstrate, we extract (observer frame) 0.6–2.0 keV band surface brightness profiles for each cluster. The expected self-similar scaling for surface brightness at fixed Δ is $S \propto kT K(z, T) E(z)^3 / (1+z)^4$ (e.g., Paper I), where K is the redshift- and temperature-dependent K-correction. Adopting this scaling, we fit a mean profile and log-normal intrinsic scatter (including covariance terms) as a function of Δ . The results are shown in Figure 2. We find a log-normal intrinsic scatter of ~ 0.25 – 0.3 at intermediate radii, $10^4 \gtrsim \Delta \gtrsim 10^3$, with increasing scatter at smaller radii. Despite the relatively large scatter, the simplicity of the mean model, which is well approximated by a power law, is appealing; in particular, these results imply that constraints on the shape of a cluster’s mass profile can in principle be obtained from surface brightness data only, by statistically associating isophotes with overdensities (as Figure 2 shows, neglecting the temperature-dependent components of the scaling increases the intrinsic scatter only marginally).¹³ In practice, the relatively large scatter at fixed Δ makes this approach less effective than traditional X-ray proxies when one only wants to estimate a total mass, which is usually the case.

¹² Pedantically speaking, neither work employs a Gaussian *process*, since the models are parametrized at a finite number of points, between which we interpolate. Nevertheless, we perpetuate this incorrect terminology in the hope that future work will move beyond these relatively limited, discrete models.

¹³ Strictly speaking, this is true only of clusters that are morphologically equivalent to those in our sample, although we expect the surface brightness template for relaxed clusters to roughly hold for the general population at intermediate-to-large radii, where earlier studies have shown approximate self-similarity of the density profiles (e.g. Vikhlinin et al. 2006; Croston et al. 2008; Paper I).

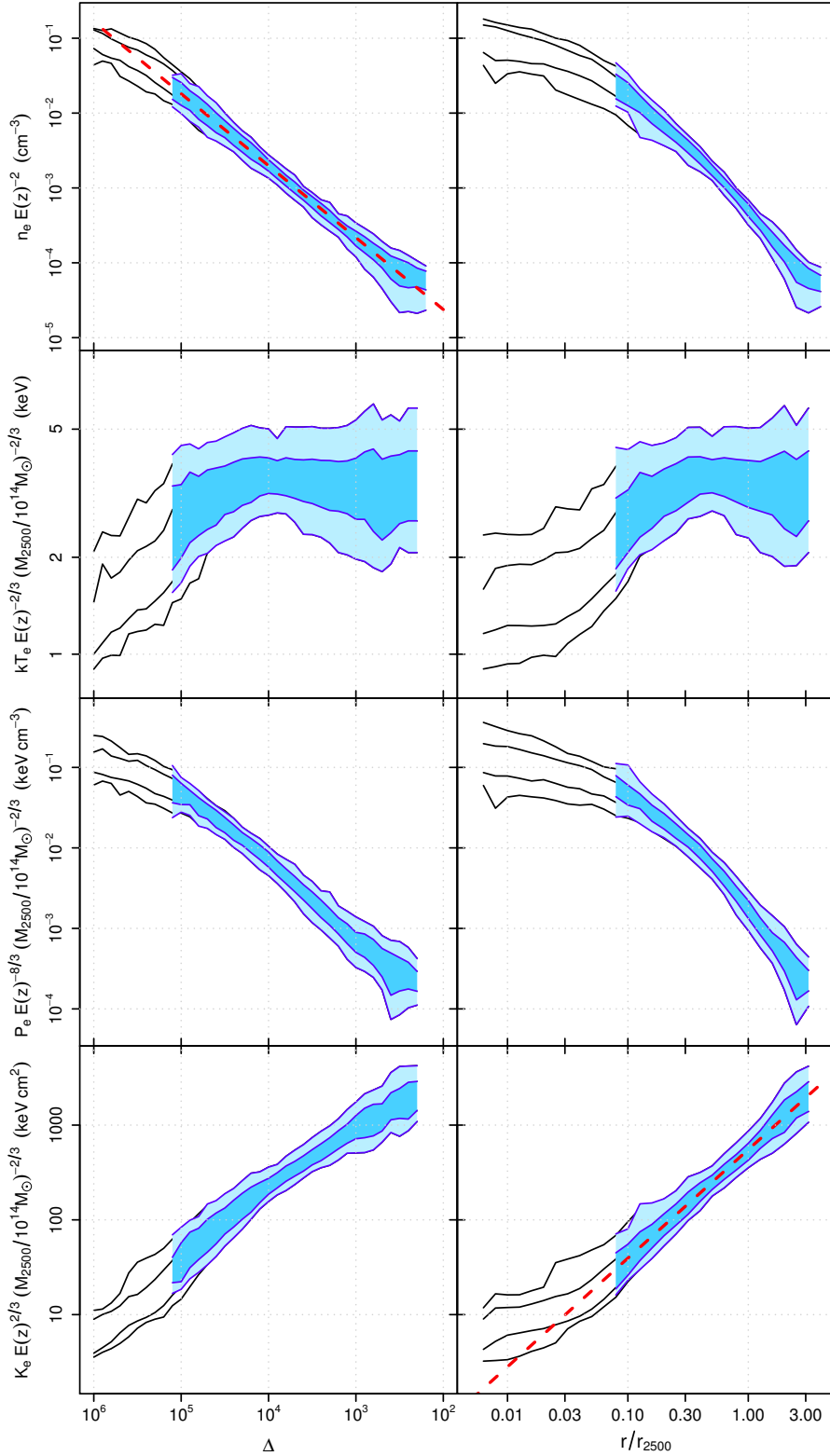


Figure 1. Profiles of electron number density, temperature, pressure and entropy, scaled according to the Kaiser (1986) model, as a function of overdensity and scaled radius. The 68.3 and 95.4 per cent confidence regions at each radius are shown, where these probabilities encompass both measurement uncertainties and intrinsic scatter among clusters in our sample. Blue lines and shading show the results when excluding the central region of each cluster (as defined in Section 2), while the results shown with black lines include the centers (where we expect larger systematic uncertainties due to asphericity). The two sets of results do not match precisely at all radii where they overlap because the central exclusion radius corresponds to different values of Δ or r/r_{2500} from cluster to cluster; hence, the two profiles differ at radii where only a subset of clusters contributes to the center-excluded results. In the upper-left and lower-right panels, the dashed lines are power-laws fit to the center-excised data, $n \propto \Delta^{0.96}$ and $K \propto (r/r_{2500})^{1.15}$.

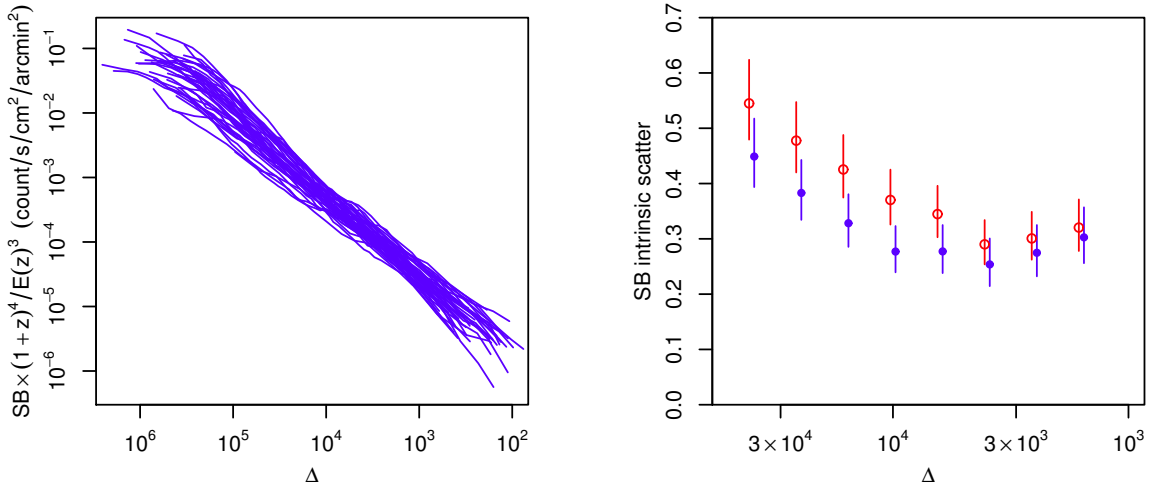


Figure 2. Left: surface brightness in the 0.6–2.0 keV band for each of our clusters, scaled with redshift as indicated. For clarity, measurement uncertainties are not shown. Right: intrinsic scatter in surface brightness at fixed overdensity. Open circles show the scatter when the profiles are scaled only by the redshift-dependent factor $E(z)^3/(1+z)^4$, as in the left panel, while filled circles show the slightly smaller scatter achievable by including the temperature-dependent scaling terms.

It has long been known that luminosities measured excluding cluster centers (by some reasonable definition) have a smaller intrinsic scatter with mass than the total luminosity (e.g., Fabian et al. 1994; Markevitch 1998; Maughan 2007; Mantz et al. 2010b). For the cluster population in general this is intuitive, since the presence or absence of a cool cores can mean as much as factor of two difference in total luminosity. The increase in surface brightness scatter at small radii, in part reflecting the evolution in the central brightness of the most relaxed clusters noted in Paper I (see also Santos et al. 2010; McDonald et al. 2013), shows that a center-excised luminosity should display reduced scatter with mass even within our morphologically similar cluster sample. As it happens, for realistic NFW concentration parameters, the inner boundary of the lowest-scatter range noted above, $\Delta \sim 10^4$, roughly corresponds to the inner radius adopted by Maughan (2007) and Mantz et al. (2010b) when defining center-excised luminosity, $0.15 r_{500}$. We return to the subject of scaling relations using integrated X-ray observables in Section 5.2.

4.2 Pressure

The shape of the ensemble pressure profile is relevant for reconstructing the integrated Compton-Y signal from Sunyaev-Zel’dovich (SZ) measurements with limited resolution (Planck Collaboration 2014), field of view (Czakon et al. 2015), or sensitivity to sufficiently large scales (Mantz et al. 2014a). To facilitate comparison with results in the literature, Figure 3 shows our ensemble pressure profile as a function of r/r_{500} . The dashed red lines in the figure show the 1σ intrinsic scatter region from a Gaussian process fit to Bolocam data (Sayers et al. 2013; similar to the fit we perform in Section 5.1). The slope of the Bolocam Gaussian process profile is in excellent agreement with ours at large radii ($\gtrsim 0.5 r_{500}$), but appears to flatten earlier at small radii; this difference can plausibly be explained by that fact that the Bolocam fit was not limited to relaxed/cool-core clusters. The gray, solid line in the figure is the gen-

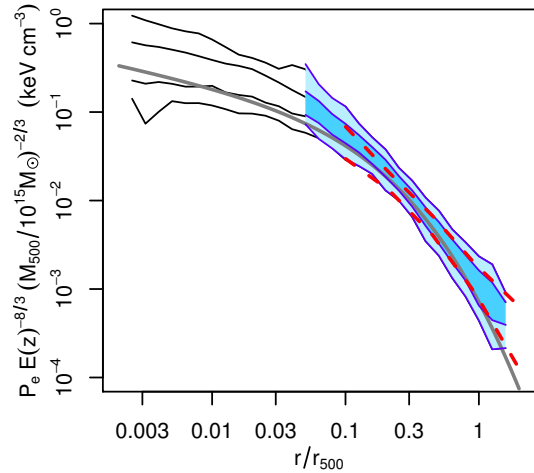


Figure 3. Scaled ensemble pressure profile as a function of r/r_{500} . The thick, gray line shows a generalized NFW fit to XMM and *Planck* data (Planck Collaboration 2013), while the dashed, red lines show the 1σ intrinsic scatter about the mean profile from a Gaussian process fit to Bolocam data (Sayers et al. 2013).

eralized NFW pressure profile for cool-core clusters from the Planck Collaboration (2013), which is fit to a combination of XMM-Newton X-ray data at small radii and *Planck* SZ data at large radii. There is an overall offset of order 10 per cent between our median pressure profile and the XMM/*Planck* profile, although they agree within our statistical+systematic uncertainties. The agreement in shape between our profile and the XMM/*Planck* results is qualitatively good over the entire radial range.

For reference, we note that our median profile is well described by

$$P(r) = 0.68 \text{ keV cm}^{-3} E(z)^{8/3} \left(\frac{M_{500}}{10^{15} M_{\odot}} \right)^{2/3} G\left(\frac{r}{r_{500}}\right), \quad (4)$$

where G is a generalized NFW function (see Nagai et al. 2007) with parameters $(P_0, c_{500}, \gamma, \alpha, \beta) = (1, 1.19, -0.01, 0.51, 4.37)$. We stress that this parametrized fit should be used only as a simple description of our results, and only over the radial range shown in the figure. In particular, the scaled profile and its intrinsic scatter from cluster to cluster are modeled in greater depth in Section 5.1.

4.3 Entropy

The ensemble entropy profile in Figure 1 displays features in common with numerous other studies of clusters and elliptical galaxies, namely a power law with radius (dashed line in the figure), flattening to a “floor” at small radii (Lloyd-Davies et al. 2000; Ponman et al. 2003; Piffaretti et al. 2005; Donahue et al. 2006; Morandi & Etti 2007; Cavagnolo et al. 2009; Pratt et al. 2010; Werner et al. 2012, 2014; Panagoulia et al. 2014; McDonald et al. 2014). We note, however, that the departure from power-law behavior is limited to radii which are excluded from our main results due to the considerations discussed in Section 2, specifically the possibility that the choice of center, ellipticity, or presence of local density fluctuations (sloshing, cavities, etc.) may bias the density profiles inferred from a spherical deprojection. The ensemble profiles in Figure 1 are relatively conservative in this regard, excluding at least the central 50 kpc, even when no disturbances in the ICM are visible.

To better probe the central regions of the clusters, we do away with this default exclusion in this section, extending the entropy profiles inwards until the radii where the specific features mentioned above appear to become significant. The resulting individual profiles (blue lines with error bars) are shown as a function of metric radius in Figure 4. Although the “undisturbed” region of several of our cluster profiles reaches as low as ~ 20 kpc (~ 0.01 – $0.02 r_{200}$), less than half the radius of the previous default exclusion, there are no strong indications of departures from a power law. Our results do not exclude the possibility of an entropy floor of radius ~ 30 kpc in cool-core clusters, as generally agreed upon in the literature. However, they do call into question the validity of this concordance, given that systematics that may affect the determination of deprojected density are present at these radii in even the most relaxed and massive clusters. We note that both Panagoulia et al. (2014) and Werner et al. (2012, 2014) present measured entropy profiles that display power-law behavior down to radii of $\lesssim 1$ kpc ($\lesssim 0.01 r_{200}$), respectively for samples of groups and highly relaxed elliptical galaxies.

The dashed, red line in Figure 4 shows the “baseline” entropy power law due to purely gravitational structure formation found from the simulations of Voit et al. (2005), which is in good agreement with more recent simulations using several different codes (e.g. Sembolini et al. 2015). Here we have scaled the baseline profile according to the median mass and redshift of our cluster sample (see Voit et al. 2005), and to account for the difference between the cluster gas-mass fraction in the simulations and that measured from our data at r_{2500} . There is good agreement between the theoretical curve and the data at radii $\gtrsim 500$ kpc, although the power-law slope of the observed profiles is somewhat shallower than the model (~ 1.15 compared with

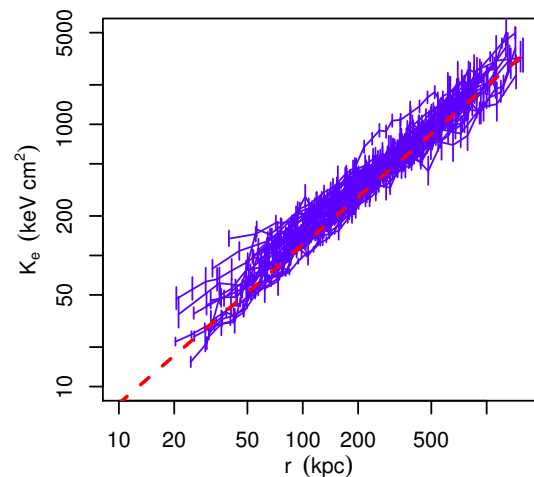


Figure 4. Profiles of entropy as a function of metric radius in our cluster sample. In this figure, the profile for each cluster is extended to the smallest radius where the ICM is undisturbed and where a spherical deprojection appears valid. With this restriction, each of the profiles shown appears consistent with a power law. The dashed line corresponds to the predicted behavior from simple hydrodynamical simulations (without cooling or feedback) scaled according to the median mass, redshift and gas mass fraction of the observed sample.

1.21), suggesting that we may be seeing some excess entropy near cluster centers.

We emphasize that a power-law entropy profile extending down to relatively small radii in this sample of dynamically relaxed clusters is compatible with the notion that cooling and feedback processes significantly affect the gas at small radii in groups and clusters. Indeed, our results in Sections 5.2 and 5.3 indicate an important role for cooling and feedback within $\sim 0.15 r_{500}$ for the massive clusters studied here. The measured entropy profiles suggest that heating and cooling in the central regions of these systems proceeds via a continuous feedback cycle that allows the central entropy profiles to remain stratified, preserving the similarity and relatively low intrinsic scatter evident in Figure 4, rather than violent episodic outbursts. Within the central 20 kpc, clear departures from spherical symmetry prevent robust thermodynamic profiles from being extracted from the data.

5 SCALING RELATIONS

We now turn to the scaling of the measured thermodynamic quantities with mass and redshift. First, in Section 5.1, we consider the scaling of the thermodynamic profiles, including their intrinsic covariance as a function of radius. Section 5.2 then considers the scaling relations of traditional integrated or global cluster measurements.

In previous work, we have stressed that scaling relations of the cluster population as a whole can only be reliably constrained when the sample selection and the underlying cosmological mass function are properly incorporated into the fitted model (Mantz et al. 2010a; Allen et al. 2011; see also Evrard et al. 2014; Czakon et al. 2015). This is impossible in the present case, since the sample selection is complex

(Paper I) and depends on features which are not yet accurately reproduced in simulations (e.g., cool cores). Among the selection criteria, the $kT > 5$ keV cut is clearly important in the context of scaling relations. Most of our clusters are also initially selected from X-ray flux limited surveys, and must satisfy a redshift-dependent cut on central surface brightness, so we might expect selection effects to influence the density or luminosity scaling relations at some level. It is less clear that the selection should affect gas masses or center-excised luminosity measurements, which are dominated by the fainter parts of a cluster. While it has been argued that marginalizing over a flexible prior on the underlying distribution of masses and redshifts, as we do, may partially mitigate these issues (Sereno & Ettori 2015), our results in this section should be interpreted as strictly empirical, and certainly only apply to relaxed clusters.

5.1 Scaling of Profiles

Using the method described in Section 3, we fit a joint model for the mean density and temperature profiles, their intrinsic covariance, and their scaling with mass and $E(z)$. In detail, this means that at a fixed set of N_Δ ordinates, $\{\Delta_i\}$, we constrain the scaled density and temperature, $n_i[E(z)/E(0.35)]^{-\beta_{nz}}(M_{2500}/3 \times 10^{14} M_\odot)^{-\beta_{nm}}$ and $kT_i[E(z)/E(0.35)]^{-\beta_{tz}}(M_{2500}/3 \times 10^{14} M_\odot)^{-\beta_{tm}}$.¹⁴ The slopes, β , are also free parameters of the fit. The model also includes a $2N_\Delta \times 2N_\Delta$ log-normal intrinsic covariance matrix, encoding the marginal cluster-to-cluster scatter in density and temperature at each Δ , the covariance of each of these quantities at each pair of overdensities (e.g., the covariance of departures from the mean density at small and large radii), and the density–temperature scatter covariance as a function of overdensity. Constraining this model requires the full set of 40 clusters to provide data at each overdensity. To ensure that this is the case, even though the mass profile of each cluster (effectively, Δ as a function of angular radius) is being marginalized over, we model only the overdensity range $10^{4.6} \geq \Delta \geq 10^{3.4}$. Table 2 summarizes the results. Note that it is straightforward to convert this model for the joint density–temperature scaling and scatter to a model for pressure, entropy, or some other product of powers of n and kT .

Figure 5 shows the 68.3 and 95.4 per cent confidence constraints on the power-law slopes of density and temperature with mass and $E(z)$. Black circles show the predictions of the self-similar model, and dashed lines correspond to varying a single exponent at a time in Equation 2 (including the implicit M^0 in the expression for n). All of the measured slopes are consistent with the self-similar model.

The right panel of Figure 5 shows the marginal intrinsic scatter in density and temperature at each overdensity. Consistent with our analysis of the surface brightness in Section 4.1, the scatter in density is largest at small radii, and

levels off at $\Delta \lesssim 10^4$. The temperature scatter shows a similar trend, and is smaller than both the scatter in the density profile and the scatter in average temperature determined in Section 5.2. The latter might be expected, given that in this section we are taking advantage of the radially resolved, 3-dimensional temperature profiles. However, we caution that the individual temperature measurements are still effectively averaged over a relatively large volume (i.e. the resolution in radius is poor) compared to the density; this might result in intrinsic scatter on smaller scales, which can be probed in density, being suppressed in the temperature profiles. A comparison to realistic hydrodynamical simulations and/or very deep, high-resolution observations could shed light on this question.

Constraints on the off-diagonal covariances of the model, in the form of correlation coefficients, are shown in Figure 6. The correlation of density at different radii appears to drop monotonically with their separation, approximately independent of their absolute position within the cluster (at least, within the modeled radial range). The same is true of temperature, albeit with larger uncertainties. This indicates that the overall scalings with mass and $E(z)$ are broadly successful in standardizing the density and temperature profiles, whereas strong correlations or anticorrelations at large separations would suggest that perhaps the scalings should be radius-dependent. The density–temperature correlations are consistent with zero with the exception of anticorrelations at small separation and small radius; this presumably reflects local pressure equilibrium even in the presence of variations in the spatial extent and magnitude of cool cores.

Overall, these results are consistent with what we would expect for the most relaxed clusters in the Universe, i.e. simple mean scalings with mass and redshift and similar profile shapes (outside the core). Expanding this kind of analysis to a more dynamically diverse cluster selection, most likely in simulations given the difficulty in measuring precise mass profiles for unrelaxed clusters, could prove interesting in the future.

5.2 Scaling of Integrated Measurements

We next turn to the more traditional scaling relations of global or integrated quantities. For this analysis, we adopt r_{500} , the most common choice in the literature, as the characteristic radius within which to make these measurements. Here the values of r_{500} are determined by our NFW analysis of each cluster, and we account for the correlation of mass and temperature at fixed radius imparted by the hydrostatic assumption as described in Section 2, as well as the straightforward correlation in measurement uncertainty between mass and other quantities measured within a mass-dependent aperture. The thermodynamic quantities we consider are the spherically integrated gas mass within r_{500} , the average temperature measured in an annulus spanning $0.15 < r/r_{500} < 1$ (as determined from a 2-temperature-bin non-parametric deprojection; see Section 2), the soft-band (0.1–2.4 keV) intrinsic luminosity projected within r_{500} , and the “center-excised” luminosity projected onto an annulus spanning 0.15 – $1 r_{500}$, denoted L_{ce} . These measurements are plotted in Figure 7, along with a representation of their covariance with mass. Using the regression technique described in Section 3 and by Mantz (2016), we simultane-

¹⁴ Note that there is no particular reason to expect departures from self-similar evolution to manifest themselves as a power-law in $E(z)$, as opposed to some other function of redshift. However, this parametrization does provide a simple and convenient null test of whether such departures exist.

Table 2. Constraints on the mean scaled electron density and temperature profiles of our sample, the power-law scaling indices of each profile with M_{2500} and $E(z)$, and the intrinsic covariance about the mean profiles. The model is given in terms of a discrete set of overdensities (as a proxy for radius), and the scaling is relative to $z = 0.35$ and $M_{2500} = 3 \times 10^{14} M_{\odot}$. The covariance is broken down into the density–density, temperature–temperature and density–temperature blocks, and expressed as marginal standard deviations along the diagonal and correlation coefficients off of the diagonal.

Mean						Slopes		
Δ	$10^{4.6}$	$10^{4.3}$	$10^{4.0}$	$10^{3.7}$	$10^{3.4}$	$E(z)$	M_{2500}	
$\ln(n/\text{cm}^{-3})$	-4.51 ± 0.05	-5.18 ± 0.04	-5.83 ± 0.03	-6.51 ± 0.03	-7.18 ± 0.03	n	2.0 ± 0.2	0.03 ± 0.06
$\ln(kT/\text{keV})$	2.007 ± 0.030	2.077 ± 0.023	2.107 ± 0.014	2.097 ± 0.014	2.073 ± 0.017	kT	0.64 ± 0.08	0.67 ± 0.02

Covariance									
	$n(\Delta_1)$	$n(\Delta_2)$	$n(\Delta_3)$	$n(\Delta_4)$	$n(\Delta_5)$	$kT(\Delta_1)$	$kT(\Delta_2)$	$kT(\Delta_3)$	$kT(\Delta_4)$
$n(\Delta_1)$	$0.32^{+0.05}_{-0.04}$					$0.15^{+0.03}_{-0.02}$	$0.78^{+0.09}_{-0.13}$	$0.46^{+0.22}_{-0.30}$	$0.33^{+0.25}_{-0.30}$
$n(\Delta_2)$	$0.93^{+0.03}_{-0.04}$	$0.25^{+0.04}_{-0.03}$				$0.11^{+0.02}_{-0.02}$	$0.58^{+0.19}_{-0.28}$	$0.45^{+0.22}_{-0.28}$	$0.23^{+0.26}_{-0.29}$
$n(\Delta_3)$	$0.87^{+0.05}_{-0.07}$	$0.92^{+0.03}_{-0.05}$	$0.18^{+0.03}_{-0.03}$				$0.05^{+0.02}_{-0.01}$	$0.44^{+0.21}_{-0.28}$	$0.29^{+0.29}_{-0.29}$
$n(\Delta_4)$	$0.70^{+0.10}_{-0.14}$	$0.79^{+0.07}_{-0.10}$	$0.84^{+0.06}_{-0.09}$	$0.17^{+0.03}_{-0.02}$				$0.06^{+0.01}_{-0.01}$	$0.39^{+0.21}_{-0.26}$
$n(\Delta_5)$	$0.37^{+0.19}_{-0.22}$	$0.47^{+0.17}_{-0.20}$	$0.55^{+0.15}_{-0.19}$	$0.70^{+0.11}_{-0.14}$	$0.16^{+0.03}_{-0.03}$				$0.07^{+0.02}_{-0.02}$
	$n(\Delta_1)$	$n(\Delta_2)$	$n(\Delta_3)$	$n(\Delta_4)$	$n(\Delta_5)$	$kT(\Delta_1)$	$kT(\Delta_2)$	$kT(\Delta_3)$	$kT(\Delta_4)$
$kT(\Delta_1)$	$-0.82^{+0.11}_{-0.07}$	$-0.77^{+0.14}_{-0.09}$	$-0.68^{+0.17}_{-0.12}$	$-0.46^{+0.22}_{-0.18}$	$-0.11^{+0.25}_{-0.24}$				
$kT(\Delta_2)$	$-0.88^{+0.09}_{-0.05}$	$-0.86^{+0.10}_{-0.06}$	$-0.81^{+0.13}_{-0.08}$	$-0.63^{+0.19}_{-0.14}$	$-0.29^{+0.25}_{-0.22}$				
$kT(\Delta_3)$	$-0.59^{+0.29}_{-0.20}$	$-0.60^{+0.30}_{-0.20}$	$-0.57^{+0.31}_{-0.21}$	$-0.50^{+0.33}_{-0.22}$	$-0.30^{+0.33}_{-0.26}$				
$kT(\Delta_4)$	$-0.44^{+0.30}_{-0.24}$	$-0.46^{+0.30}_{-0.24}$	$-0.47^{+0.30}_{-0.24}$	$-0.42^{+0.32}_{-0.25}$	$-0.23^{+0.33}_{-0.28}$				
$kT(\Delta_5)$	$-0.21^{+0.29}_{-0.27}$	$-0.21^{+0.30}_{-0.28}$	$-0.23^{+0.30}_{-0.28}$	$-0.20^{+0.32}_{-0.30}$	$-0.09^{+0.31}_{-0.31}$				

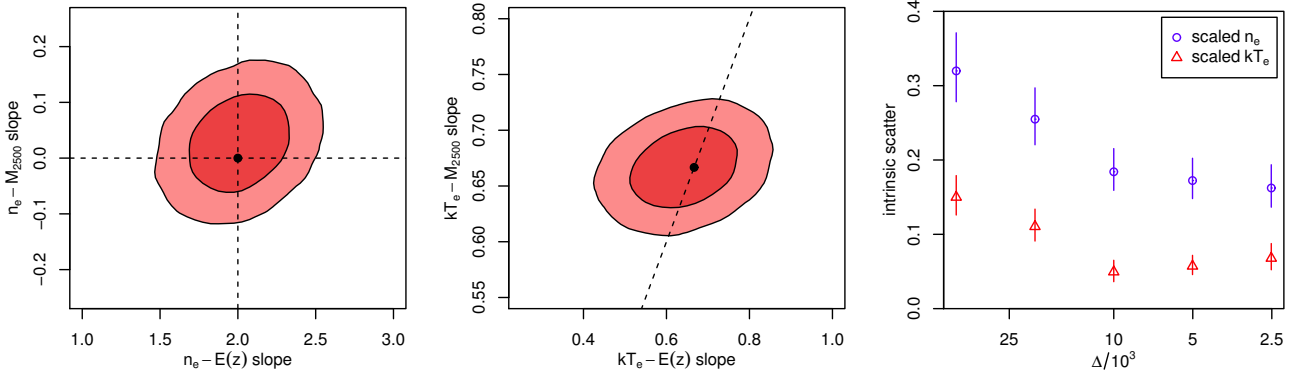


Figure 5. Left and center: constraints (68.3 and 95.4 per cent confidence) on power-law slopes of the overall scaling of gas density and temperature profiles with mass and $E(z)$. The self-similar expectation is indicated by filled black circles, and dashed lines show the effect of changing a single exponent at a time in Equation 2. Right: marginal intrinsic scatters of density and temperature at the modelled set of overdensities (see Table 2).

ously fit for the scaling of these 4 variables as a function of M_{500} and $E(z)$, including their 4×4 intrinsic covariance matrix. For completeness, we also include below some results for the luminosity projected within a radius of $0.15 r_{500}$ ($L_{\text{core}} = L - L_{\text{ce}}$), although the computationally singular correlations among the three luminosity measurements prevent us from fitting all 5 scaling relations simultaneously.

Figure 8 and Table 3 show constraints on each of the scaling relation slopes. The gas mass and temperature slopes are all consistent with self-similarity, as expected from our analysis of the density and temperature profile scalings in Section 5.1.¹⁵ However, the scaling of total luminosity is not

consistent with self-similarity, preferring either a weaker dependence on redshift, a stronger dependence on mass, or both, consistent with a number of previous results (e.g., Reiprich & Böhringer 2002; Zhang et al. 2007, 2008; Mantz et al. 2008, 2010b; Rykoff et al. 2008; Pratt et al. 2009; Vikhlinin et al. 2009; Leauthaud et al. 2010; Reichert et al. 2011; Sereno & Ettori 2015; see also the review of Giodini et al. 2013). This is a clearly radius-dependent phenomenon, with L_{ce} being perfectly consistent with self-similarity, L_{core} preferring stronger departures from self-similarity, and the total luminosity occupying a middle ground. While the un-

¹⁵ We note in particular that the steep $M_{\text{gas}}-M$ slopes inferred from some analyses of dynamically heterogeneous systems, ex-

tending down to the group scale, e.g., Pratt et al. 2009; Sun et al. 2009) are not consistent with the results reported here for the most massive, dynamically relaxed systems.

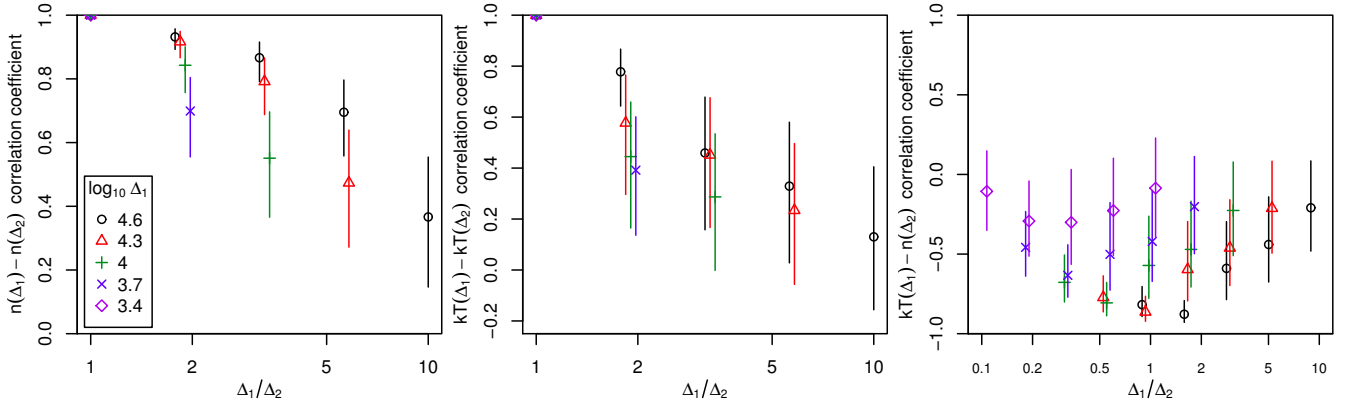


Figure 6. Correlation coefficients of the joint density–temperature intrinsic covariance, plotted as a function of separation in overdensity units. n – n and kT – kT correlations appear to drop with separation in a roughly translation-invariant way. The kT – n correlations are all approximately consistent with zero except at small radii (large $\Delta_1 \approx \Delta_2$). Small horizontal offsets are introduced to make the plots clearer.

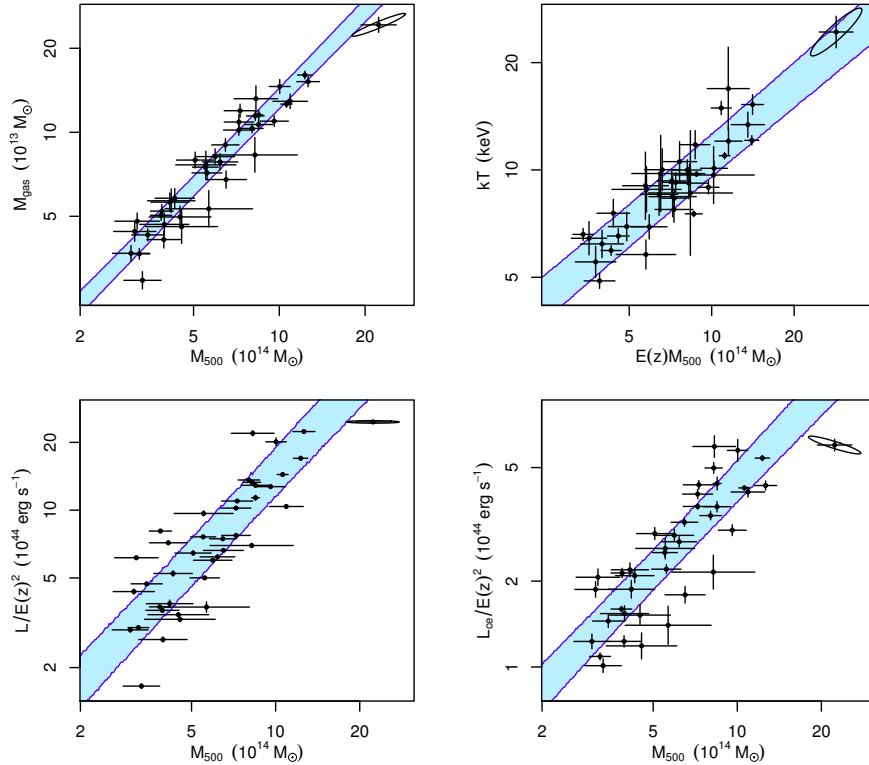


Figure 7. Scatter plots summarizing the integrated thermodynamic quantities for which we fit scaling relations with M_{500} and $E(z)$. In each panel, the measurement covariance ellipse is shown for the most massive cluster in the sample. Shaded regions show the 1σ predictions for a subset of the model space we explore, specifically with the power of $E(z)$ fixed to 0.0 (for M_{gas}) or 2.0 (for L and L_{ce}), or required to be equal to the power of M_{500} (for kT).

certainty on the evolution of L_{core} is substantial, milder than self-similar evolution is qualitatively consistent with the decreasing central surface brightness of cool-core clusters with redshift seen by Santos et al. (2008, 2010) and McDonald et al. (2013), and in Paper I.

Constraints on the intrinsic covariances of the model appear in Figure 9 and Table 4. Our constraints on the marginal scatter of M_{gas} and kT are largely consistent with earlier work (see Allen et al. 2011; Giodini et al. 2013, and

references therein); in particular the small scatter in M_{gas} , 0.086 ± 0.023 is similar to the scatter found for f_{gas} in a shell spanning radii 0.8 – $1.2 r_{2500}$ in Paper II, 0.074 ± 0.023 (see also Section 5.3; Allen et al. 2008). The kT scatter, 0.134 ± 0.019 , agrees well with results for the cluster population at large (e.g., Arnaud et al. 2007; Vikhlinin et al. 2009; Mantz et al. 2010b). As one would expect, given the intentional morphological similarity of the clusters in our sample, we measure a scatter in total luminosity at fixed

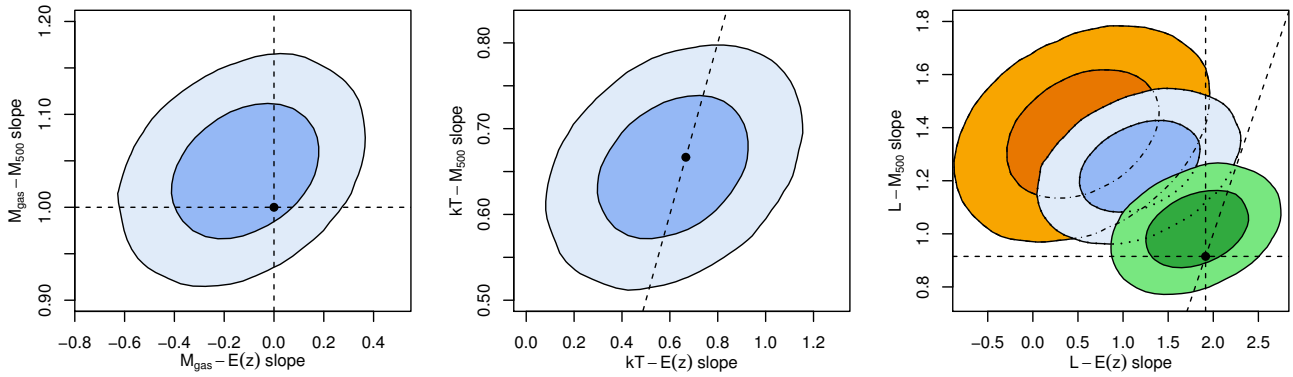


Figure 8. Constraints on the power-law slopes of the scaling relations of integrated gas mass, temperature and luminosity as a function of mass and $E(z)$. The self-similar expectation is indicated by filled black circles, and dashed lines show the effect of changing a single exponent at a time in Equation 3. In the right panel, blue shading corresponds to the slopes for total luminosity (L), green shading corresponds to those for L_{ce} , and orange shading corresponds to L_{core} .

Table 3. Constraints on the power-law slopes of the scaling relations of gas mass, temperature and luminosity (integrated within r_{500}) as a function of mass and $E(z)$. Normalizations are given as the natural logarithm of the listed quantities at $z = 0.35$ and $M_{500} = 6 \times 10^{14} M_{\odot}$.

	normalization	$E(z)$ slope	M_{500} slope
M_{gas}/M_{\odot}	31.98 ± 0.02	-0.11 ± 0.18	1.04 ± 0.05
kT/keV	2.18 ± 0.02	0.61 ± 0.20	0.66 ± 0.05
$L/\text{erg s}^{-1}$	103.70 ± 0.05	1.20 ± 0.43	1.26 ± 0.11
$L_{ce}/\text{erg s}^{-1}$	102.66 ± 0.04	1.82 ± 0.35	1.02 ± 0.09

mass, 0.24 ± 0.05 , that is smaller than that of the population at large (~ 0.4 ; e.g., Vikhlinin et al. 2009; Mantz et al. 2010b). However, even with this selection, the scatter in L_{core} is still significant, $0.34^{+0.06}_{-0.05}$. The scatter in L_{ce} is smaller than that in the total luminosity, although at low confidence, 0.17 ± 0.05 .

Although the sample employed here is relatively small, we are nevertheless able to place constraints on the off-diagonal terms relating M_{gas} , kT , L and L_{ce} . Our constraint on the kT - L correlation coefficient is -0.06 ± 0.24 . The M_{gas} - kT correlation is constrained at a similar level, -0.18 ± 0.28 , consistent with zero. In contrast, the M_{gas} - L correlation prefers positive values, $0.43^{+0.22}_{-0.30}$, reflecting the fact that these quantities are both essentially integrals of the same gas density profile, but with different weighting. The correlation between M_{gas} and L_{ce} is very strong, $0.88^{+0.06}_{-0.16}$; correspondingly, the correlations of kT and L with L_{ce} are similar to the M_{gas} - kT and M_{gas} - L correlations.¹⁶ There have been few previous measurements of the off-diagonal terms of the cluster scaling relation intrinsic scatter. Mantz et al. (2010b) measured the correlation of L and kT at fixed mass to be 0.09 ± 0.19 (not restricted to relaxed clusters), consistent with our findings above. Rozo et al. (2010) placed a lower limit on the correlation of L and M at fixed optical richness (as defined for the MaxBCG catalog) of > 0.85 .

¹⁶ The strength of the M_{gas} - L_{ce} correlation explains why Mantz et al. (2010b), using M_{gas} as a proxy for total mass, found a smaller intrinsic scatter in L_{ce} than we do ($\lesssim 10$ per cent).

More recently, Maughan (2014) fit L_{ce} , kT and M_{gas} scaling relations, including intrinsic scatter covariances although without modeling measurement covariances, to published data for REXCESS clusters. Those results on the intrinsic correlation coefficients are compatible with, and have similar precision to, our constraints from relaxed clusters.

Overall, the picture that emerges is one in which the gas temperature and density outside of the core, roughly at radii 0.15 – $1 r_{500}$, behaves simply and in accordance with the self-similar model for these massive, relaxed clusters. In particular, the strong correlation in scatter between M_{gas} and L_{ce} requires the gas density profiles to be smooth at these radii (Figure 1; recall that the absence of substructure on these scales is a requirement of the sample selection in Paper I), since scatter in density is reflected disproportionately in the luminosity compared to the gas mass. In the centers of relaxed clusters, we see breaking of the self-similar model, specifically in the form of enhanced intrinsic scatter in luminosity, and a preference for scaling relation slopes of core luminosity with mass (redshift) that are steeper (shallower) than the self-similar prediction. These results require the action of a non-self-similar astrophysical process such as AGN feedback (Fabian 2012; McNamara & Nulsen 2012, and references therein), although in general both heating and cooling processes may contribute to the observed trends.

The product of gas mass and temperature, $Y_X = M_{gas}kT$, has been used extensively as a mass proxy in recent years (e.g., Maughan 2007; Vikhlinin et al. 2009; Andersson et al. 2011; Menanteau et al. 2012; Benson et al. 2013; Brodwin et al. 2016). Given a power-law plus log-normal scatter model, the Y_X scaling relation and its scatter can be derived directly from our results for the M_{gas} and kT scaling relations, and their intrinsic covariance. The constraints on the Y_X slopes appear in the left panel of Figure 10, and are consistent with self-similarity (since M_{gas} and kT are, individually). In principle, masses estimated from such a combination can be no more precise than estimates from the individual measurements, accounting for the full intrinsic covariance matrix.¹⁷ Nevertheless, we show in the right

¹⁷ Note, however, that part of the motivation for using Y_X is due to the fact that, in simulations, it appears to be less sensitive

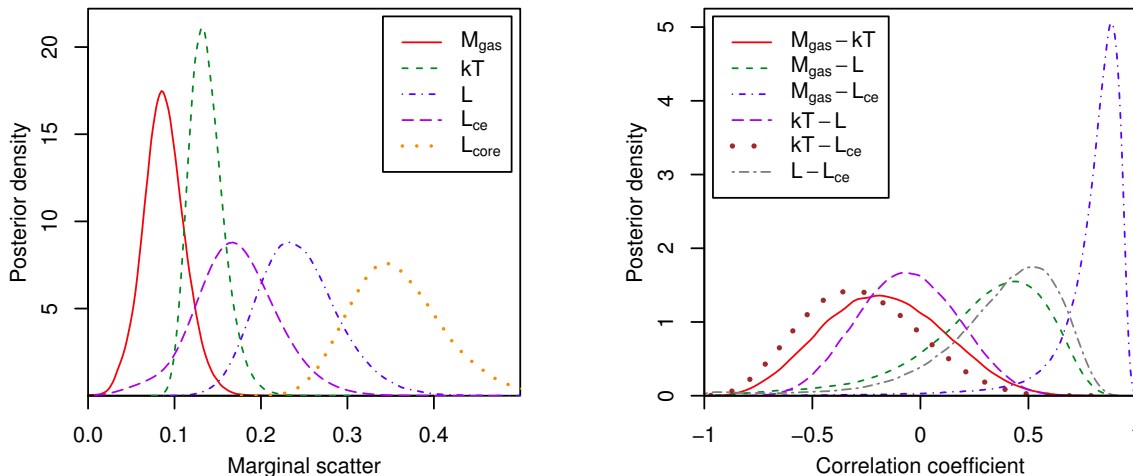


Figure 9. Marginal scatters (left) and correlation coefficients (right), respectively representing the diagonal and off-diagonal elements of the intrinsic covariance of integrated M_{gas} , kT , L and L_{ce} at fixed M_{500} and $E(z)$. The marginal scatter of central luminosity is also shown in the left panel.

Table 4. Constraints on the marginal scatters (on-diagonal entries) and correlation coefficients (off-diagonal entries), respectively representing the diagonal and off-diagonal elements of the intrinsic covariance of integrated M_{gas} , kT , L and L_{ce} at fixed M_{500} and $E(z)$.

	M_{gas}	kT	L	L_{ce}
M_{gas}	0.09 ± 0.02			
kT	-0.18 ± 0.28	0.13 ± 0.02		
L	$0.43^{+0.22}_{-0.30}$	-0.06 ± 0.24	0.24 ± 0.05	
L_{ce}	$0.88^{+0.06}_{-0.16}$	-0.30 ± 0.27	$0.53^{+0.17}_{-0.29}$	0.17 ± 0.05

panel of Figure 10 the intrinsic scatter in mass corresponding to products of observables of the form $kT^\alpha Y^{2-\alpha}$, where Y is one of M_{gas} , L or L_{ce} , accounting for the intrinsic correlation or anticorrelation of the observables as measured above (e.g., Stanek et al. 2010).¹⁸ We see that choosing an optimal combination of observables, or simply using their intrinsic covariance as measured above, produces modestly smaller scatter compared to the individual observables involved. Neglecting uncertainties, the intrinsic scatter of mass with the combination $kT^{0.51} M_{\text{gas}}^{1.49}$ is 0.072, compared with 0.084 with M_{gas} alone or 0.21 with kT alone. Combining kT with L_{ce} yields smaller gains, predictably, with the product $kT^{1.05} L_{\text{ce}}^{0.95}$ yielding a mass scatter of 0.11, and $kT^{1.25} L^{0.75}$ yielding a scatter of 0.14. While it is difficult to improve on the small intrinsic scatter of M_{gas} in the regime of our cluster sample, we note that the combination of temperature and luminosity (especially L_{ce}) is competitive. What proxy or proxies are most useful in practice also depends on the size of the statistical and systematic uncertainties of each

measurement; being weighted towards smaller radii, L_{ce} is generally measured with smaller uncertainty than M_{gas} at r_{500} , which in turn has smaller statistical and systematic uncertainties than the temperature at r_{500} (Figure A1).

5.3 Scaling of f_{gas}

Paper II presented limited results on the scaling of f_{gas} , specifically f_{gas} in a spherical shell spanning 0.8–1.2 r_{2500} , and on the intrinsic scatter of f_{gas} in a few such shells when assuming no scaling with mass. Here we provide a more comprehensive treatment, differing from Paper II in the version of the *Chandra* calibration used and the consistent use of the same model employed in previous sections, i.e. including free power-law slopes with both mass and $E(z)$ as well as intrinsic scatter. These results provide a more complete picture of how the intracluster medium is redistributed, relative to the self-similar model, due to astrophysical processes.

Figure 11 shows constraints on the power-law slope of f_{gas} with M_{2500} and the intrinsic scatter for a series of spherical shells of radial width 0.4 r_{2500} . In interpreting these plots, it must be stressed that the results across shells are non-trivially correlated due to the common M_{2500} values used in the regression, as well as the use of a parametrized mass profile. Nevertheless, it is clear that the gas mass fraction at small cluster radii increases with mass, while at larger radii ($\gtrsim 0.8 r_{2500}$) the slope is consistent with zero. As observed in Paper II, the intrinsic scatter is minimized at radii $\sim r_{2500}$, clearly increasing towards smaller radii. The average f_{gas} in each shell closely traces the differential profiles

to dynamical state and closer to a power-law in mass (extending to poor clusters and groups) than M_{gas} or kT individually (Kravtsov et al. 2006). Our sample, being restricted to massive, relaxed clusters by construction, cannot test these features.

¹⁸ We have chosen to have the exponents in this combination sum to 2 for convenience, but note that the mass scatter is invariant to this choice, depending only on the relative contributions of kT and Y . The minimum of each curve in the figure is the scatter one would obtain by using the individual observables and directly accounting for their intrinsic covariance.

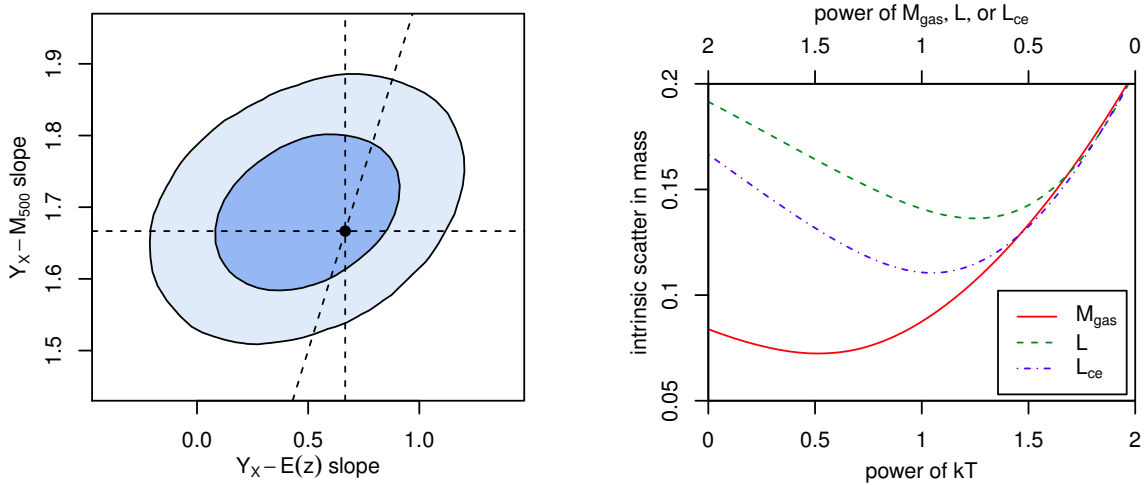


Figure 10. Left: Constraints on the power-law slopes of $Y_X = M_{\text{gas}} kT$ as a function of mass and $E(z)$, as in Figure 8. Right: intrinsic scatter in mass from products of observables of the form $kT^\alpha Y^{2-\alpha}$, where Y is one of M_{gas} , L or L_{ce} .

shown in Paper II (Figure 2), while the power-law slope with $E(z)$ is consistent with zero at the $\sim 1\sigma$ level in each shell. Table 5 shows the constraints on the fit parameters for a subset of the shells, as well as for f_{gas} in full spheres bounded by r_{2500} and r_{500} (the latter from Section 5.2) fit with the same model.

The fact that the gas mass fractions of clusters increase with radius and are well below the cosmic average in their inner regions (e.g. Allen et al. 2002, 2004, 2008; Vikhlinin et al. 2006; Paper II) provides some of the clearest evidence for feedback (even more so in galaxies; e.g. McNamara & Nulsen 2012). In contrast, hydrodynamic simulations without cooling or feedback predict a constant gas mass fraction as a function of mass and radius (Borgani & Kravtsov 2011 and references therein). Beyond this simple comparison, the results in Figure 11 and Table 5 complement those of Section 5.2 in demonstrating that the gas distribution at small cluster radii has a larger scatter and greater dependence on mass than the gas properties at larger radii (in this case gas mass rather than luminosity). Interestingly, even though f_{gas} in the shell radially centered at r_{2500} is constant with respect to M_{2500} , f_{gas} integrated in a sphere bounded by r_{2500} displays an increasing slope with mass, 0.10 ± 0.05 , due to the influence of the central regions. When integrating over the larger region bounded by r_{500} , this slope is consistent with zero. Note that we do not expect this result to apply to significantly less massive clusters or at the group scale, where the astrophysical processes that break self-similarity in the centers of our clusters may show their influence at larger radii (e.g. Sun et al. 2009). We also note that both of the spherically integrated measurements retain a larger intrinsic scatter, due to the inclusion of cluster centers, than the asymptotic value of ~ 0.07 seen in the shells at $r \gtrsim 0.6 r_{2500}$. As noted in Paper II, the small intrinsic scatter in the $0.8\text{--}1.2 r_{2500}$ shell, combined with the typically good signal-to-noise at these radii in *Chandra* data, directly translates into improved cosmological constraints compared with a larger-scatter observable. The independence of mass of the f_{gas} in this shell is appealingly simple, although in principle a mass dependence can easily be incorporated into the full cosmological model (see discussion in Paper II).

6 CONCLUSION

We present profiles of density and temperature (and the derived quantities pressure and entropy) for a sample of 40 massive, dynamically relaxed galaxy clusters, and provide the first constraints on the scaling with mass and redshift of these profiles, including their intrinsic covariance as a function of radius. We also fit scaling relations of traditional, integrated quantities: gas mass, average temperature, total soft-band luminosity, and center-excluded luminosity. This analysis includes the full multivariate intrinsic covariance matrix, and our results represent the first constraints on some of these cross terms.

Whether in terms of profiles or aperture-integrated measurements, our results support a picture in which the ICM in these massive, relaxed clusters follows self-similar scaling laws, with the exception of their innermost centers (radii $\lesssim 0.15 r_{500}$). The luminosity (i.e., gas density) in these central regions evolves less strongly, and has a stronger dependence on mass, than the self-similar prediction, consistent with the physical effects expected from the development of cool cores and heating by central AGN. Even in this morphologically selected sample of relaxed clusters, cluster centers dominate the intrinsic scatter in X-ray luminosity at fixed mass and redshift. The center-excised luminosity has a smaller scatter, ~ 15 per cent, comparable to that of the average temperature. For these clusters, gas mass has the smallest intrinsic scatter, ~ 8 per cent, although an optimal combination of gas mass and temperature can also serve well as a total mass proxy. Consistent with the results above and in Paper II, we find that a shell spanning $\sim 0.8\text{--}1.2 r_{2500}$ is near optimal for cosmological studies using f_{gas} , due to the small scatter of the gas mass fraction at these radii.

Within the centers of our clusters, the measured trends in luminosity and the gas mass fraction indicate redistribution of the ICM by non-gravitational processes such as cooling and feedback. At the same time, the measured entropy profiles remain regular, with small scatter, down to the smallest radii where deprojected measurements can be robustly made ($20 \text{ kpc} \sim 0.01 r_{200}$). The results suggest that the heating and cooling processes at work in the centers of

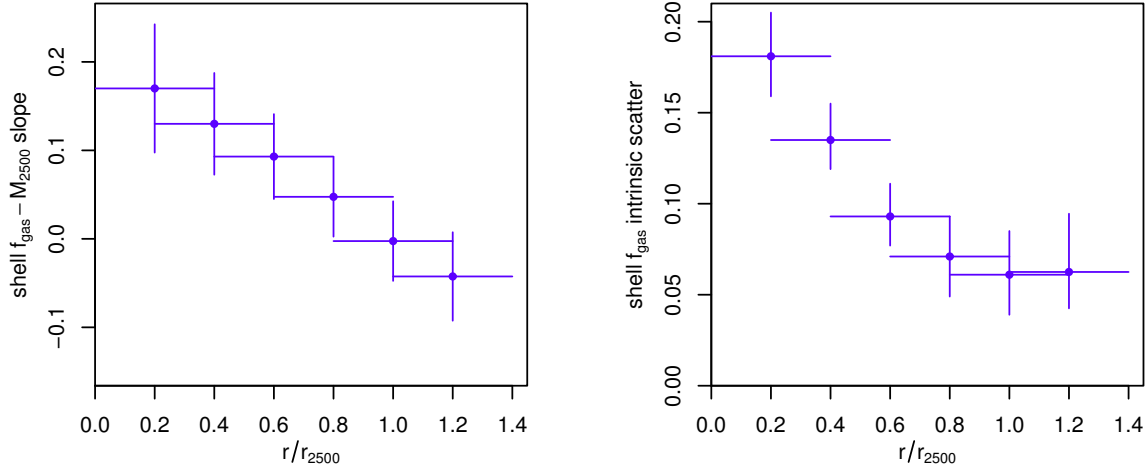


Figure 11. Constraints on the power-law scaling with mass (left) and intrinsic scatter (right) of f_{gas} measured in spherical shells. Horizontal bars indicate the radial extent of the regions where f_{gas} is measured, while vertical bars show 68.3 per cent confidence intervals. Note that the plotted points are non-trivially correlated; nevertheless, the gross trends are clear. As a function of increasing radius, out to $\sim 1.2 r_{2500}$, the slope of f_{gas} with mass systematically decreases, becoming consistent with zero at $r \gtrsim 0.8 r_{2500}$. The intrinsic scatter decreases to a minimum at $\sim r_{2500}$, and appears to flatten beyond that.

Table 5. Constraints on the gas-mass fraction and its scaling properties in various spherical shells. The first two columns show the inner and outer radii of each shell in units of r_{2500} (however the outer radius for the last line is actually r_{500} rather than a strict multiple of r_{2500}). The third column shows the model constraint on f_{gas} in each shell at $z = 0.35$ and $M_{2500} = 3 \times 10^{14} M_{\odot}$, and columns 4–5 show the constraints on power-law indices with mass and $E(z)$. Column 6 shows the intrinsic scatter in $\ln(f_{\text{gas}})$ at fixed mass and redshift.

r_{in}	r_{out}	f_{gas}	$E(z)$ slope	M_{2500} slope	scatter
0.0	0.4	0.082 ± 0.002	-0.38 ± 0.27	0.17 ± 0.07	0.18 ± 0.02
0.4	0.8	0.105 ± 0.002	-0.14 ± 0.17	0.09 ± 0.05	0.09 ± 0.02
0.8	1.2	0.129 ± 0.002	-0.15 ± 0.17	0.00 ± 0.05	0.06 ± 0.02
0.0	1.0	0.100 ± 0.002	-0.17 ± 0.18	0.10 ± 0.05	0.11 ± 0.02
0.0	~ 2.2	0.129 ± 0.003	-0.11 ± 0.18	0.04 ± 0.05	0.09 ± 0.02

massive clusters are tightly coupled, allowing the gas to remain stratified on these scales.

ACKNOWLEDGEMENTS

We acknowledge support from the U.S. Department of Energy under contract number DE-AC02-76SF00515, and from the National Aeronautics and Space Administration (NASA) through *Chandra* Award Numbers GO8-9118X and TM1-12010X, issued by the *Chandra* X-ray Observatory Center, which is operated by the Smithsonian Astrophysical Observatory for and on behalf of NASA under contract NAS8-03060. ABM also received support from the National Science Foundation under grant AST-1140019.

REFERENCES

- Allen S. W., Evrard A. E., Mantz A. B., 2011, [ARA&A](#), **49**, 409
- Allen S. W., Rapetti D. A., Schmidt R. W., Ebeling H., Morris R. G., Fabian A. C., 2008, [MNRAS](#), **383**, 879
- Allen S. W., Schmidt R. W., Ebeling H., Fabian A. C., van Speybroeck L., 2004, [MNRAS](#), **353**, 457
- Allen S. W., Schmidt R. W., Fabian A. C., 2002, [MNRAS](#), **334**, L11
- Andersson K. et al., 2011, [ApJ](#), **738**, 48
- Applegate D. E. et al., 2016, [MNRAS](#), in press, [arXiv:1509.02162](#)
- Applegate D. E. et al., 2014, [MNRAS](#), **439**, 48
- Arnaud M., Pointecouteau E., Pratt G. W., 2007, [A&A](#), **474**, L37
- Benson B. A. et al., 2013, [ApJ](#), **763**, 147
- Borgani S., Kravtsov A., 2011, [Adv. Sci. Lett.](#), **4**, 204
- Brodwin M., McDonald M., Gonzalez A. H., Stanford S. A., Eisenhardt P. R., Stern D., Zeimann G. R., 2016, [arXiv:1504.01397](#)
- Cavagnolo K. W., Donahue M., Voit G. M., Sun M., 2009, [ApJS](#), **182**, 12
- Croston J. H. et al., 2008, [A&A](#), **487**, 431
- Czakon N. G. et al., 2015, [ApJ](#), **806**, 18

- Donahue M., Horner D. J., Cavagnolo K. W., Voit G. M., 2006, *ApJ*, **643**, 730
- Evrard A. E., Arnault P., Huterer D., Farahi A., 2014, *MNRAS*, **441**, 3562
- Fabian A. C., 2012, *ARA&A*, **50**, 455
- Fabian A. C., Crawford C. S., Edge A. C., Mushotzky R. F., 1994, *MNRAS*, **267**, 779
- Giodini S., Lovisari L., Pointecouteau E., Ettori S., Reiprich T. H., Hoekstra H., 2013, *Space Sci. Rev.*, **177**, 247
- Kaiser N., 1986, *MNRAS*, **222**, 323
- Kelly B. C., 2007, *ApJ*, **665**, 1489
- Kelly P. L. et al., 2014, *MNRAS*, **439**, 28
- Kravtsov A. V., Vikhlinin A., Nagai D., 2006, *ApJ*, **650**, 128
- Leauthaud A. et al., 2010, *ApJ*, **709**, 97
- Lloyd-Davies E. J., Ponman T. J., Cannon D. B., 2000, *MNRAS*, **315**, 689
- Mantz A., Allen S. W., Ebeling H., Rapetti D., 2008, *MNRAS*, **387**, 1179
- Mantz A., Allen S. W., Ebeling H., Rapetti D., Drlica-Wagner A., 2010b, *MNRAS*, **406**, 1773
- Mantz A., Allen S. W., Rapetti D., Ebeling H., 2010a, *MNRAS*, **406**, 1759
- Mantz A. B., 2016, *MNRAS*, in press, arXiv:1509.00908
- Mantz A. B. et al., 2014a, *ApJ*, **794**, 157
- Mantz A. B., Allen S. W., Morris R. G., Rapetti D. A., Applegate D. E., Kelly P. L., von der Linden A., Schmidt R. W., 2014b, *MNRAS*, **440**, 2077
- Mantz A. B., Allen S. W., Morris R. G., Schmidt R. W., von der Linden A., Urban O., 2015, *MNRAS*, **449**, 199
- Markevitch M., 1998, *ApJ*, **504**, 27
- Maughan B. J., 2007, *ApJ*, **668**, 772
- Maughan B. J., 2014, *MNRAS*, **437**, 1171
- McDonald M. et al., 2014, *ApJ*, **794**, 67
- McDonald M. et al., 2013, *ApJ*, **774**, 23
- McNamara B. R., Nulsen P. E. J., 2012, *New Journal of Physics*, **14**, 055023
- Menanteau F. et al., 2012, *ApJ*, **748**, 7
- Morandi A., Ettori S., 2007, *MNRAS*, **380**, 1521
- Nagai D., Kravtsov A. V., Vikhlinin A., 2007, *ApJ*, **668**, 1
- Nagai D., Vikhlinin A., Kravtsov A. V., 2007, *ApJ*, **655**, 98
- Navarro J. F., Frenk C. S., White S. D. M., 1997, *ApJ*, **490**, 493
- Panagoulia E. K., Fabian A. C., Sanders J. S., 2014, *MNRAS*, **438**, 2341
- Piffaretti R., Jetzer P., Kaastra J. S., Tamura T., 2005, *A&A*, **433**, 101
- Planck Collaboration, 2014, *A&A*, **571**, A29
- Planck Collaboration, 2013, *A&A*, **550**, A131
- Ponman T. J., Sanderson A. J. R., Finoguenov A., 2003, *MNRAS*, **343**, 331
- Pratt G. W. et al., 2010, *A&A*, **511**, A85
- Pratt G. W., Croston J. H., Arnaud M., Böhringer H., 2009, *A&A*, **498**, 361
- Reichert A., Böhringer H., Fassbender R., Mühlegger M., 2011, *A&A*, **535**, A4
- Reiprich T. H., Böhringer H., 2002, *ApJ*, **567**, 716
- Rozo E. et al., 2010, *ApJ*, **708**, 645
- Rykoff E. S. et al., 2008, *MNRAS*, **387**, L28
- Santos J. S., Rosati P., Tozzi P., Böhringer H., Ettori S., Bignamini A., 2008, *A&A*, **483**, 35
- Santos J. S., Tozzi P., Rosati P., Böhringer H., 2010, *A&A*, **521**, A64
- Sayers J. et al., 2013, *ApJ*, **768**, 177
- Sembolini F. et al., 2015, arXiv:1503.06065
- Sereno M., Ettori S., 2015, *MNRAS*, **450**, 3675
- Stanek R., Rasia E., Evrard A. E., Pearce F., Gazzola L., 2010, *ApJ*, **715**, 1508
- Sun M., Voit G. M., Donahue M., Jones C., Forman W., Vikhlinin A., 2009, *ApJ*, **693**, 1142
- Vikhlinin A. et al., 2009, *ApJ*, **692**, 1033
- Vikhlinin A., Kravtsov A., Forman W., Jones C., Markevitch M., Murray S. S., Van Speybroeck L., 2006, *ApJ*, **640**, 691
- Voit G. M., Kay S. T., Bryan G. L., 2005, *MNRAS*, **364**, 909
- von der Linden A. et al., 2014, *MNRAS*, **439**, 2
- Werner N., Allen S. W., Simionescu A., 2012, *MNRAS*, **425**, 2731
- Werner N. et al., 2014, *MNRAS*, **439**, 2291
- Zhang Y.-Y., Finoguenov A., Böhringer H., Kneib J.-P., Smith G. P., Czoske O., Soucail G., 2007, *A&A*, **467**, 437
- Zhang Y.-Y., Finoguenov A., Böhringer H., Kneib J.-P., Smith G. P., Kneissl R., Okabe N., Dahle H., 2008, *A&A*, **482**, 451

APPENDIX A: INDIVIDUAL CLUSTER PROFILES

Figure A1 shows the deprojected temperature and electron density profiles of each individual cluster in our sample, as determined from the non-parametric spectral fits (red/orange crosses in each panel) and the fits that assume an NFW mass profile (blue shaded boxes and lines with errors). Note that the choice of a deprojection center to optimize symmetry of the emission on large scales may result in biases in the density and temperature at very small radii. For this reason, the cluster centers are excluded from the NFW fits, and there are no corresponding solutions for densities and temperatures in those regions (from the NFW model). Confidence intervals at the 68.3 and 95.4 per cent level are shown, with the exception of the density profiles from the NFW model, where only 95.4 per cent intervals are shown. Vertical dashed lines show the best-fitting value of r_{2500} for each cluster. Radii expressed in kpc and densities are dependent on our adopted reference cosmological model. See Section 2 for more details.

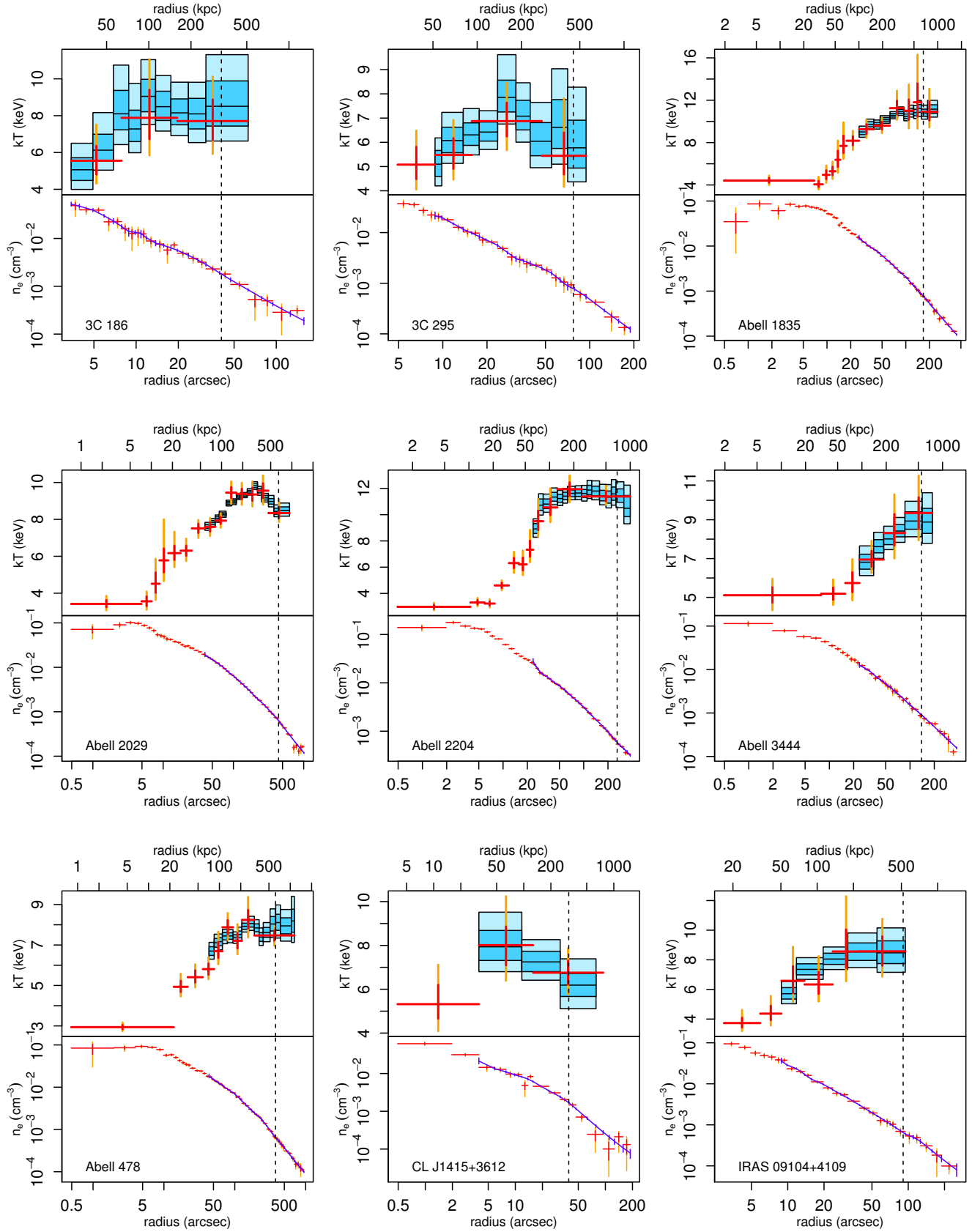
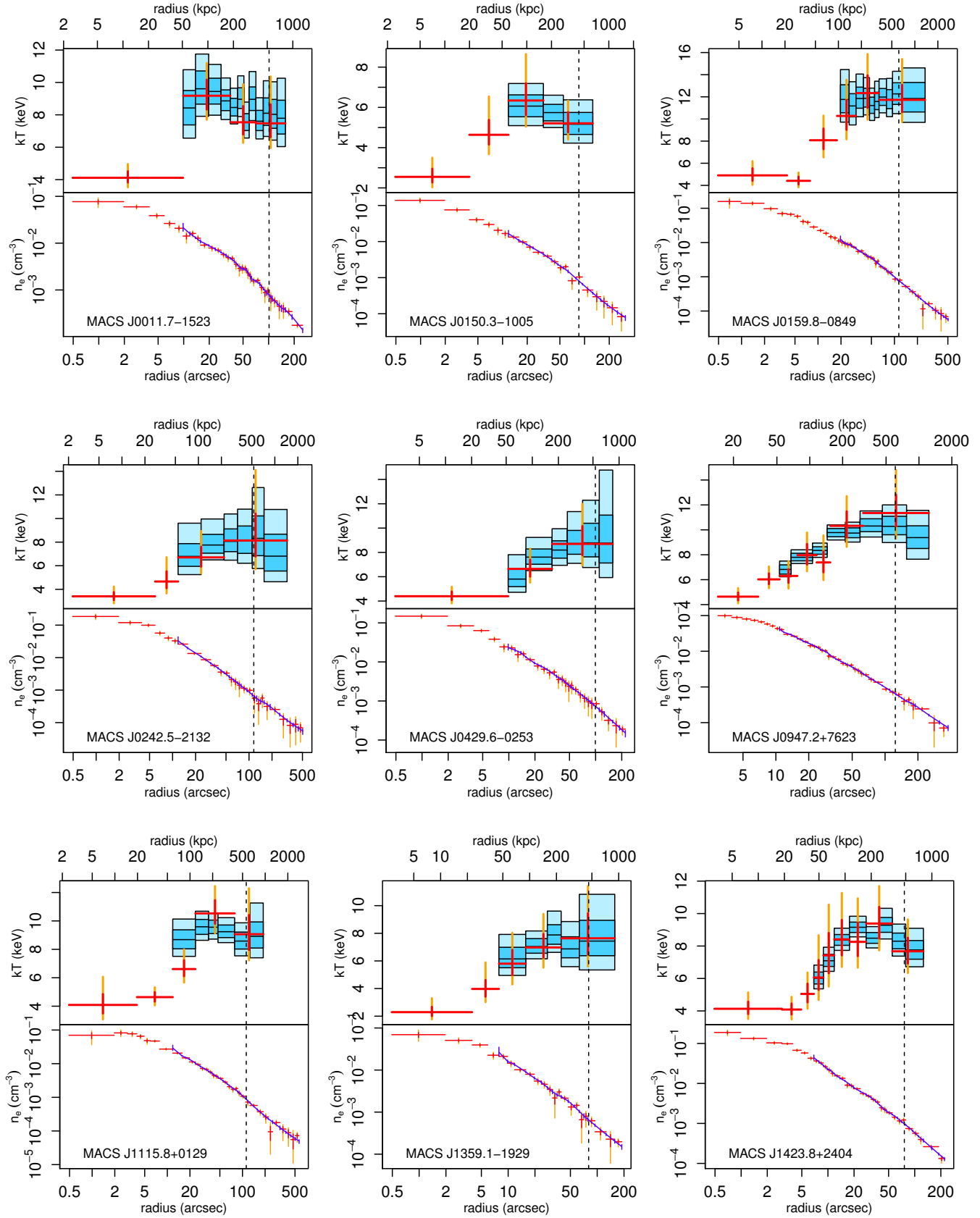


Figure A1.

Figure A1 – *continued*

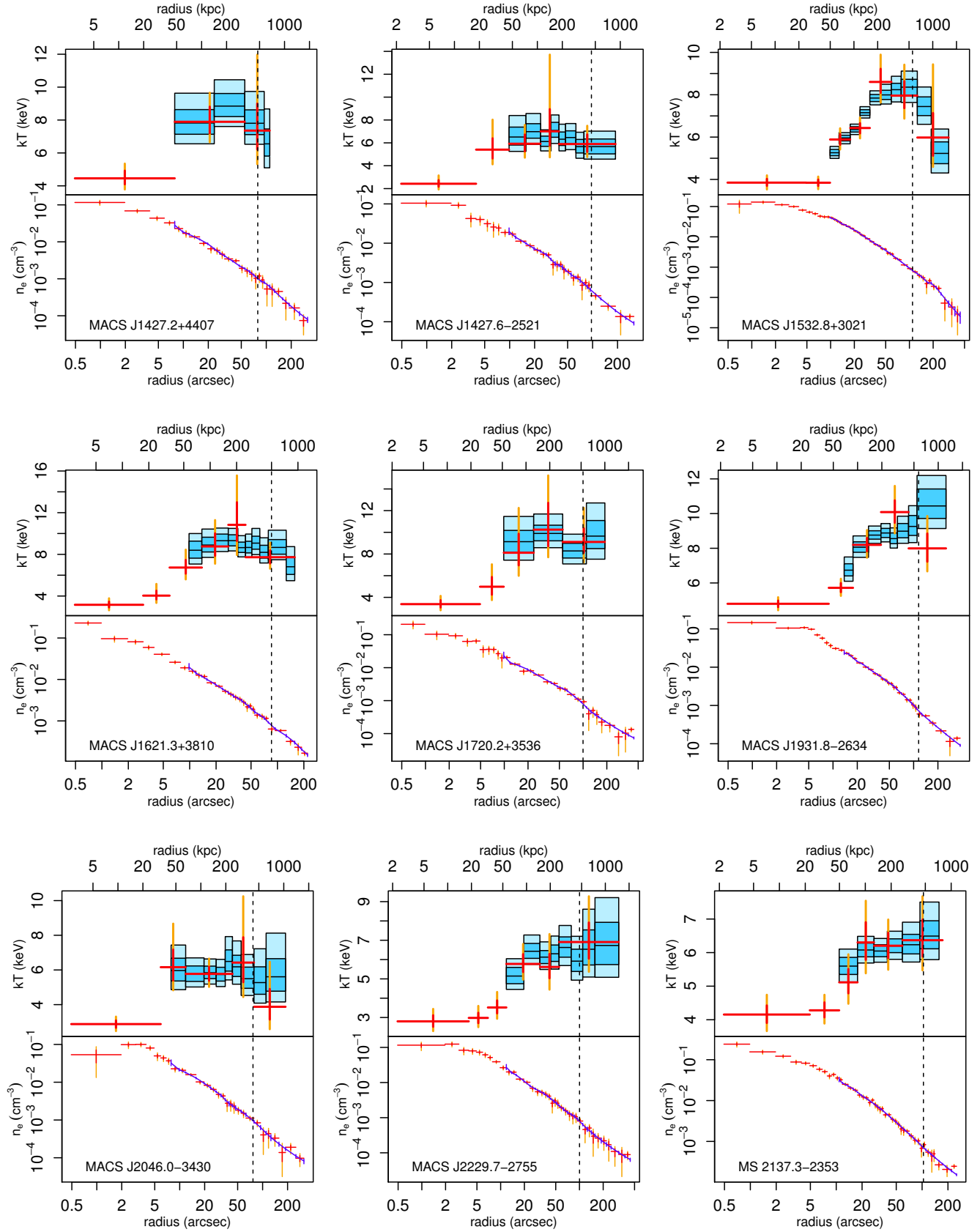


Figure A1 – continued

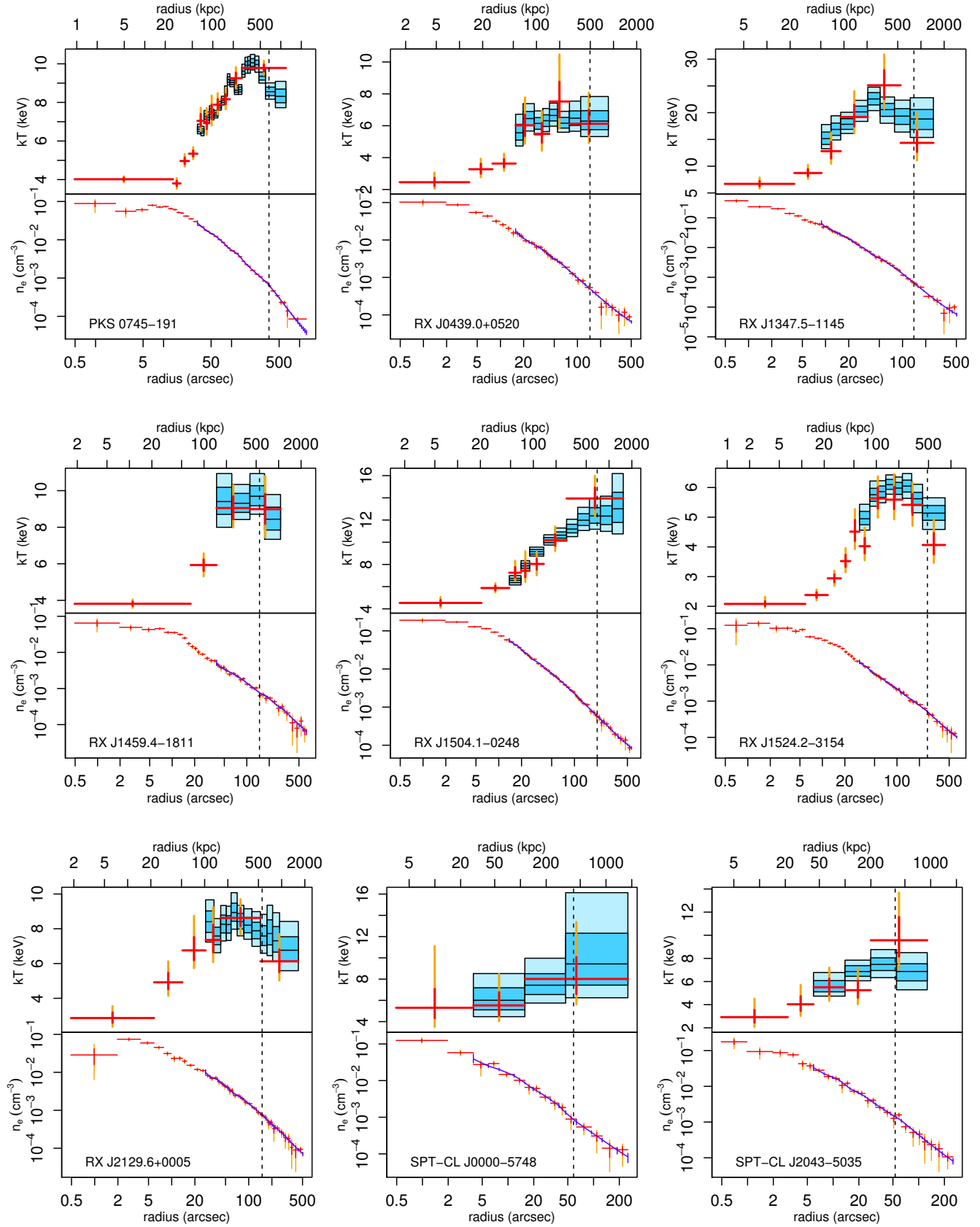


Figure A1 – continued

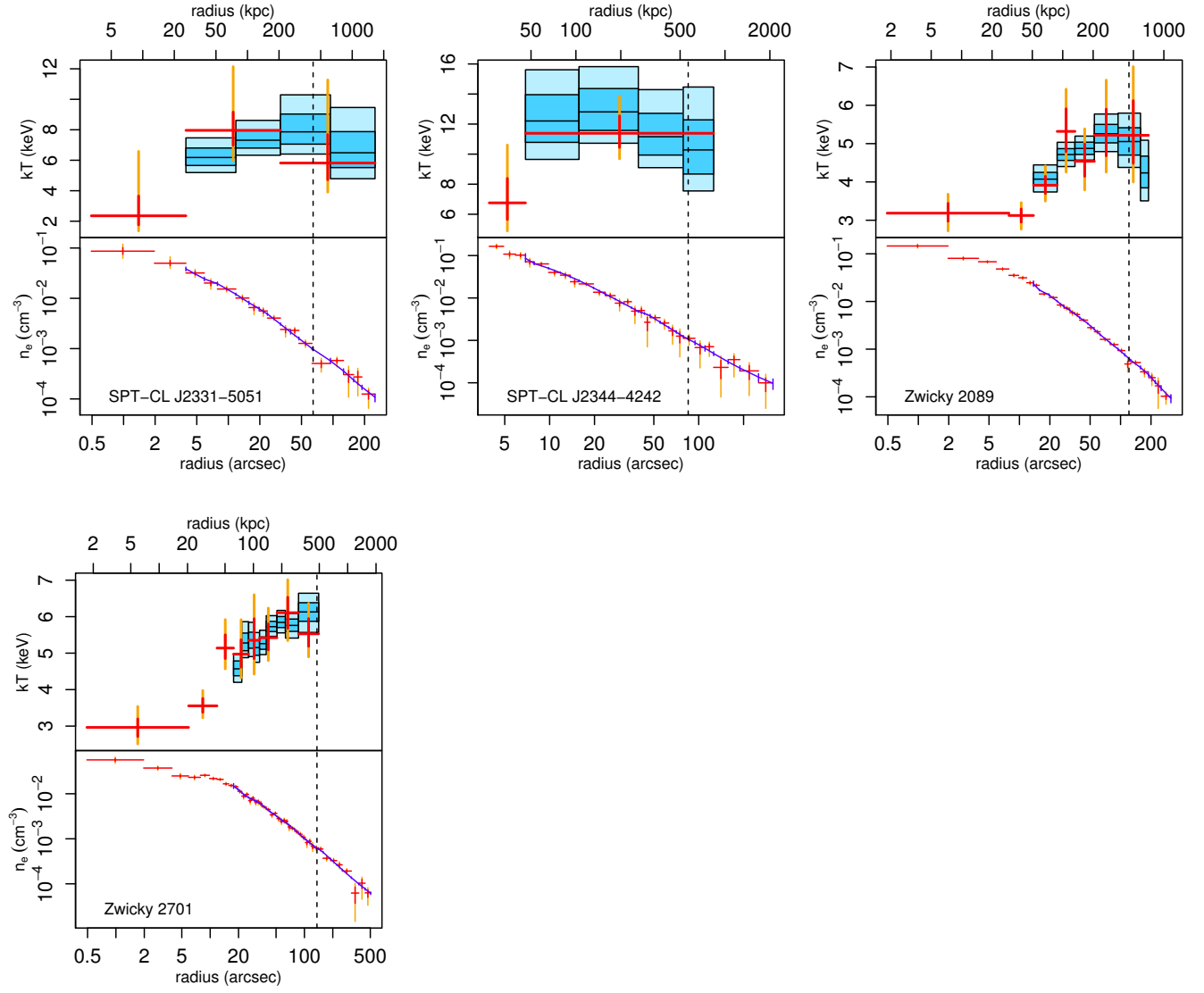


Figure A1 – continued